

# Leveraging Normalizing Flows for Orbital-Free Density Functional Theory

Alexandre de Camargo,<sup>†</sup> Ricky T. Q. Chen,<sup>‡</sup> and Rodrigo A. Vargas-Hernández<sup>\*,†,¶</sup>

<sup>†</sup>*Department of Chemistry and Chemical Biology, McMaster University, Hamilton, ON, Canada*

<sup>‡</sup>*FAIR at Meta, NY, USA*

<sup>¶</sup>*Brockhouse Institute for Materials Research, McMaster University, Hamilton, ON, Canada*

E-mail: [vargashr@mcmaster.ca](mailto:vargashr@mcmaster.ca)

## Abstract

Orbital-free density functional theory (OF-DFT) for real-space systems has historically depended on Lagrange optimization techniques, primarily due to the inability of previously proposed electron density approaches to ensure the normalization constraint. This study illustrates how leveraging contemporary generative models, notably normalizing flows (NFs), can surmount this challenge. We develop a Lagrangian-free optimization framework by employing these machine learning models for the electron density. This diverse approach also integrates cutting-edge variational inference techniques and equivariant deep learning models, offering an innovative reformulation to the OF-DFT problem. We demonstrate the versatility of our framework by simulating a one-dimensional diatomic system, LiH, and comprehensive simulations of hydrogen, lithium hydride, water, and four hydrocarbon molecules. The inherent flexibility of NFs facilitates initialization with promolecular densities, markedly enhancing the efficiency of the optimization process.

*Introduction:* The density functional theory (DFT) framework has evolved into an indispensable tool in both computational materials science and chemistry, with the Kohn-Sham (KS) formalism being the de facto (or most com-

monly employed) form of DFT<sup>1–4</sup>. The success of the KS formalism sparked a race to develop exchange-correlation (XC) energy functionals based on electronic spin densities<sup>5–11</sup>. Initially, physics-motivated functionals were the predominant framework until machine learning (ML) approaches emerged, marking a noteworthy shift in the landscape of quantum chemistry<sup>12–17</sup>.

Orbital-free DFT (OF-DFT), rooted in the Hohenberg-Kohn theorems<sup>18,19</sup>, is a promising alternative to KS-DFT given its lower computational scaling. However, the imperative for relative accuracy in kinetic energy (KE) functionals, comparable to the total energy, remains a primary impediment<sup>20,21</sup>. Research endeavors have extensively explored the parametrization of KE functionals<sup>22–24</sup>, surpassing the original Thomas-Fermi-Weizsäcker-based formulation. Notable extensions involve non-local KE functionals based on linear response theory, such as the Wang-Teter<sup>25</sup>, Perrot<sup>26</sup>, Wang-Govind-Carter<sup>27</sup>, Huang-Carter<sup>28</sup>, Smargiassi-Madden<sup>29</sup>, Foley-Madden<sup>30</sup> and Mi-Genova-Pavanello<sup>31</sup> functionals, showcasing the capability of OF-DFT in simulating systems with a large number of atoms.

Similar to the development of XC functionals, the pursuit of highly accurate OF-DFT simulations has driven the development of KE functionals through ML algorithms. Predominant approaches employ kernel ridge regres-

sion<sup>32</sup>, convolutional neural networks<sup>33</sup>, and ResNets<sup>34</sup>. Notably, data used for training ML-based KE functionals are generated through KS-based simulations. However, a key limitation in data-driven functionals lies in the accuracy of functional derivatives, which, when poor, can result in highly inaccurate densities. Despite significant recent progress in materials modeling within the OF-DFT framework, which now includes ML techniques, a consistent aspect for real-space simulations has been the parametrized form of the trial electron density. These traditional approaches have forced the OF-DFT framework to be a Lagrangian-based scheme. In this work, we propose an alternative approach employing generative models, specifically normalizing flows, circumventing the normalization constraints that affect traditional methods in the OF-DFT real-space setup. Our research is motivated by previous efforts that aim to develop unconstrained optimization methods for computational chemistry<sup>35–39</sup>.

*Methods:* In the OF-DFT framework, the ground state energy ( $E_{\text{gs}}$ ) and electron density ( $\rho_{\mathcal{M}}$ ) are determined by minimizing the total energy functional ( $E[\rho_{\mathcal{M}}]$ ),

$$E_{\text{gs}} = \inf_{\rho_{\mathcal{M}} \in \Omega} E[\rho_{\mathcal{M}}(\mathbf{x})], \quad (1)$$

$$\Omega = \left\{ \rho_{\mathcal{M}} : \rho_{\mathcal{M}} \in X, \int \rho_{\mathcal{M}}(\mathbf{x}) d\mathbf{x} = N_e \right\},$$

where  $X$  is the admissible class of physically realizable densities for  $\rho_{\mathcal{M}}$ , satisfying the normalization constraint on the total number of particles  $N_e$ . The OF-DFT framework’s resemblance to variational inference in machine learning<sup>40</sup> lies in their shared objective of approximating/learning a density distribution through an optimization/minimization procedure. All previously proposed methodologies belong to the category of density models known as “energy-based models”<sup>41,42</sup>. For instance,  $\rho_{\mathcal{M}} = f_{\phi}^2(\mathbf{x}) / \int f_{\phi}^2(\mathbf{x}) d\mathbf{x}$  or  $\rho_{\mathcal{M}} = e^{-f_{\phi}(\mathbf{x})} / \int e^{-f_{\phi}(\mathbf{x})} d\mathbf{x}$ . Common approaches for  $f_{\phi}$  include multi-grid<sup>43</sup> and wavelet frameworks<sup>44</sup>, as well as a linear combination of atomic Gaussian basis sets<sup>45</sup>; here  $\phi$  is referred as model’s parameters. Although these frameworks are robust, they require the inclusion of a Lagrange multiplier ( $\mu$ ) in the minimization

objective,

$$\min_{\rho_{\mathcal{M}}} E[\rho_{\mathcal{M}}(\mathbf{x})] - \mu \left( \int \rho_{\mathcal{M}}(\mathbf{x}) d\mathbf{x} - N_e \right), \quad (2)$$

where  $\mu$  is referred to as the chemical potential and is associated with the normalization constraint on  $N_e$ . Typically, conventional methods for solving for  $\rho_{\mathcal{M}}$  in real space involve self-consistent procedures based on functional derivatives, resulting in the Euler–Lagrange equation  $\delta E[\rho_{\mathcal{M}}(\mathbf{x})] / \delta \rho_{\mathcal{M}}(\mathbf{x}) - \mu = 0$ <sup>19</sup>.

In this work, we introduce an alternative parameterization of the electron density,

$$\rho_{\mathcal{M}}(\mathbf{x}) := N_e \rho_{\phi}(\mathbf{x}), \quad (3)$$

where  $\rho_{\phi}$  is a normalizing flow (NF) model and is also referred to as the *shape factor*<sup>19,46</sup>. This NF-based model allows us to reframe the OF-DFT variational problem as a Lagrangian-free optimization problem for molecular densities in real space, as the normalization is guaranteed by  $\rho_{\phi}$ .

In machine learning, NFs are common methodologies used for data generation and density estimation. These generative models transform a base (simple) density distribution  $\rho_0$  into a target (complex) density distribution ( $\rho_{\phi}$ ) by leveraging the change of variables formula,

$$\rho_{\phi}(\mathbf{x}) = \rho_0(\mathbf{z}) |\det \nabla_{\mathbf{z}} T_{\phi}(\mathbf{z})|^{-1}, \quad (4)$$

where  $T_{\phi}$  is a bijective transformation<sup>1</sup>. Eq. (4) guarantees the preservation of volume in the density transformation, while also allowing the computation of the target density in a tractable manner, making NFs a promising candidate for parameterizing  $\rho_{\mathcal{M}}$ . Additionally, automatic differentiation tools will enable the computation of high-order gradients of  $\rho_{\mathcal{M}}$ , commonly required in density functionals.

The proposed framework is rooted in optimal transport and measure theory where  $\rho_{\phi}$  is known as the *push-forward* of  $\rho_0$  by the function  $T_{\phi}$ , denoted by  $\rho_{\phi} = T_{\phi} \star \rho_0$ <sup>47</sup>. In the context of generative models,  $T_{\phi}$  is learned by minimiz-

<sup>1</sup> $T_{\phi} : \mathbb{R}^D \rightarrow \mathbb{R}^D$  is called a diffeomorphism, and it must be bijective, differentiable, and invertible.



ing metrics that measure the difference between the data distribution and the generative model. Here,  $T_\phi$  will be optimized/learned by minimizing total energy functional, Eqs. 1-2.

In NFs, a common approach to parametrize  $T_\phi$  is through a composition of functions;  $T_\phi = T_K \circ \dots \circ T_1$ <sup>47-49</sup>. These composable transformations can be considered as a flow discretized over time. Discrete-time NFs were originally adapted by Cranmer et al.<sup>50</sup> for  $L^2$ -Norm functions, making them well-suited for simulating quantum systems. Subsequent research has embraced this framework, exploring its applications across diverse domains. For instance, excited vibrational states of molecules<sup>51</sup>, quantum Monte Carlo simulations<sup>52-55</sup>, and more recently for KS-DFT<sup>56</sup>.

An alternative formulation of Eq. 4, proposed by Chen et al.<sup>57</sup> and referred to as continuous normalizing flows (CNF), is centered around the computation of the log density, the score function ( $\nabla_{\mathbf{x}} \log \rho(\mathbf{x})$ ), and  $T_\phi$  through a joint ordinary differential equation,

$$\partial_t \begin{bmatrix} \mathbf{z}(t) \\ \log \rho_\phi(\mathbf{z}(t)) \\ \nabla \log \rho_\phi \end{bmatrix} = \begin{bmatrix} \mathbf{g}_\phi(\mathbf{z}(t), t) \\ -\nabla \cdot \mathbf{g}_\phi(\mathbf{z}(t), t) \\ -\nabla^2 \mathbf{g}_\phi - (\nabla \log \rho_\phi)^T (\nabla \mathbf{g}_\phi(\mathbf{z}(t), t)) \end{bmatrix} \quad (5)$$

where “ $\nabla \cdot$ ” denotes the divergence operator<sup>58</sup>.  $\nabla_{\mathbf{x}} \rho(\mathbf{x})$  can be computed using the “log-derivative trick”, express as  $\nabla_{\mathbf{x}} \log \rho(\mathbf{x}) = \nabla_{\mathbf{x}} \rho(\mathbf{x}) / \rho(\mathbf{x})$ . Note that, unlike discrete-time normalizing flows, this continuous-time formulation allows for the simultaneous computation of the samples, the density, and the score function, making it convenient for evaluating density functionals. The joint computation of  $[\mathbf{z}(t), \log \rho_\phi(\mathbf{z}(t)), \nabla \log \rho_\phi]$  is achieved by solving an augmented ODE (Eq. 5), composed of three terms one for each component. For more details regarding normalizing flows, we encourage the reader to consult Refs.<sup>47,48</sup>, and Section S.1 in the Supporting Information (SI).

Commonly, the total energy functional is composed of the addition of individual functionals,

$$E[\rho_{\mathcal{M}}] = T[\rho_{\mathcal{M}}] + V_{\text{H}}[\rho_{\mathcal{M}}] + V_{\text{e-N}}[\rho_{\mathcal{M}}] + E_{\text{XC}}[\rho_{\mathcal{M}}], \quad (6)$$

where  $T$  is the KE functional,  $V_{\text{H}}$  is the Hartree potential,  $V_{\text{e-N}}$  is the electron-nuclei interaction

potential, and  $E_{\text{XC}}$  is the so-called exchange and correlation (XC) functional. For this work, the KE functional is the sum of the Thomas-Fermi (TF) and Weizsäcker (W) functionals,  $T[\rho_{\mathcal{M}}] = T_{\text{TF}}[\rho_{\mathcal{M}}] + \lambda_0 T_{\text{W}}[\rho_{\mathcal{M}}]$ , where the phenomenological parameter  $\lambda_0$  was set to 0.2<sup>45</sup>. Other KE functionals are compatible with the proposed framework as long as they are differentiable. The analytic equations of all functionals used here are reported in the SI.

For the proposed approach, all individual density functionals are rewritten in terms of an expectation over the base distribution ( $\rho_0$ )<sup>49,59</sup>,

$$\begin{aligned} F[\rho_{\mathcal{M}}] &= \int f(\mathbf{x}, \rho_{\mathcal{M}}, \nabla \rho_{\mathcal{M}}) \rho_{\mathcal{M}}(\mathbf{x}) d\mathbf{x} \\ &= (N_e)^p \int f(\mathbf{x}, \rho_\phi, \nabla \rho_\phi) \rho_\phi(\mathbf{x}) d\mathbf{x} \end{aligned}$$

$$F[\rho_{\mathcal{M}}] = (N_e)^p \mathbb{E}_{\rho_0}[f(T_\phi(\mathbf{z}), \rho_\phi, \nabla \rho_\phi)], \quad (7)$$

where  $(N_e)^p$  is the constant factor related to the number of electrons where  $p \in \mathbb{R}^+$ , and  $f(\mathbf{x}, \rho_\phi, \nabla \rho_\phi)$  is the integrand of the density functional  $F[\rho_{\mathcal{M}}]$ . For all Monte Carlo (MC) estimates of the density functionals, the samples were drawn from the base distribution<sup>2</sup> and transformed by a CNF (Eq. 5),  $\mathbf{x} = T_\phi(\mathbf{z}) := \mathbf{z} + \int_{t_0}^T \mathbf{g}_\phi(\mathbf{z}(t), t) dt$ ; see Fig. 1 and Section S.2 of the SI. We take a minibatch of samples and use Eq. 7 to construct an unbiased stochastic estimator of any density functional<sup>49</sup>.

For the optimization of  $\rho_{\mathcal{M}}$  (Eq. 2), one could use automatic differentiation to evaluate the gradient of the energy functional by differentiating through the numerical integration scheme. However, given the size of integration grids, this approach is resource-demanding and could lead to out-of-memory errors on many devices<sup>56</sup>, particularly for the  $V_{\text{H}}$  potential where a double integral is required.

By reframing the OF-DFT problem as variational inference, we can use Eq. 7 to compute the expectation value of the energy functional and its gradient with respect to the model parameters<sup>49,59</sup>,  $\nabla_\phi E[\rho_{\mathcal{M}}] \approx \mathbb{E}_{\rho_0}[\nabla_\phi f(T_\phi(\mathbf{z}), \rho_\phi, \nabla \rho_\phi)]$ , while guaranteeing the normalization constraint. Additionally, by integrating Eq. 5 in the forward direction (noise-to-data), we can generate samples from the base

<sup>2</sup>samples were drawn from  $\rho_0$ ;  $\mathbf{z} \sim \rho_0$

distribution, and evaluate the density and its score function together. This approach supplies all the necessary components for evaluating a density functional, Fig. 1. Furthermore, our framework also allows using modern stochastic gradient optimization methods to minimize the total energy, homologous to existing variational inference algorithms<sup>40,49</sup>. All required gradients were computed using the adjoint sensitivity method, as detailed in Ref.<sup>57</sup>, in JAX<sup>60</sup>, and the code developed for this work is available in the following repository.

For a more accurate energy computation using CNFs standard quantum chemistry numerical integration techniques are beneficial. First, we integrate Eq. 5 in the reverse direction (data-to-noise), mapping  $\mathbf{x}$  (grid point) to the base distribution space ( $\mathbf{z}$ ). This step is feasible because Eq. 5 has a block structure, where only the first term is necessary to compute  $\mathbf{z}$  from  $\mathbf{x}$ ;  $\mathbf{z} = T_\phi^{-1}(\mathbf{x}) := \mathbf{x} + \int_T^{t_0} g_\phi(\mathbf{z}(t), t) dt$ . Given the known value of  $\mathbf{z}$ , we compute the density and score function of the base distribution. Then, we integrate the equation forward in time, mirroring the training process, to evaluate the density functionals; Fig. 1. Combining these steps, we can compute the total energy, however, the complexity of these processes explains why directly differentiating numerical integration schemes for CNFs during training may not scale efficiently for larger systems.

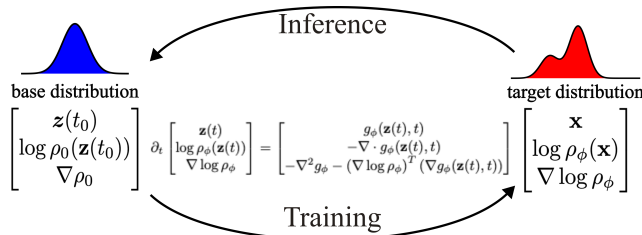


Figure 1: Continuous normalizing flows diagram.

In the context of our work, it is pertinent to note the application of automatic differentiation, a fundamental tool in the numerical ecosystem of deep learning libraries, and more recently in computational chemistry simulations<sup>61–69</sup>. In OF-DFT simulations, noteworthy examples include PROFESS-AD<sup>70</sup>, and Ref.<sup>71</sup>, where functional derivatives, crucial for optimizing the

electron density, were computed using PyTorch.

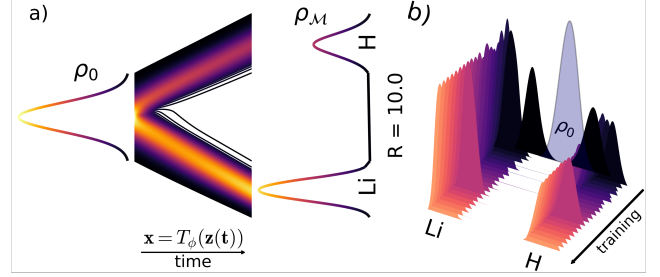


Figure 2: (a) The learned flow, Eq. 5, that minimizes the total energy for the LiH 1D system for  $R = 10$  a.u. (b) The change of  $\rho_M$  at different iterations of the optimization.  $\rho_0$  is a zero-centered Gaussian distribution. See the text for more details of the simulations.

*Results:* To illustrate the parametrization of  $\rho_M$  through a CNF, we first considered a one-dimensional (1D) model for diatomic molecules based on Ref.<sup>72</sup>. For this toy system, we considered the XC functional from Ref.<sup>73</sup>, and  $T_W$  was computed using the score function through Eq. 5,  $T_W[\rho_M] = \frac{\lambda_0}{8} \int (\nabla \log \rho_M(x))^2 \rho_M(x) dx$ . The Hartree ( $V_H$ ), and the external potentials ( $V_{e-N}$ ) both are defined by their soft version,<sup>72</sup>

$$V_H[\rho_M] = \int \int \frac{\rho_M(x) \rho_M(x')}{\sqrt{1+|x-x'|^2}} dx dx', \quad (8)$$

$$V_{e-N}[\rho_M] = - \int \left( \frac{Z_\alpha}{\sqrt{1+|x-R/2|^2}} + \frac{Z_\beta}{\sqrt{1+|x+R/2|^2}} \right) \rho_M(x) dx. \quad (9)$$

We chose LiH as the 1D diatomic molecule given the asymmetry due to the mass difference between its atoms;  $Z_\alpha = 3$ ,  $Z_\beta = 1$ . We first considered the inter-atomic distance ( $R$ ) equal to 10 Bohr. For the estimation of the total energy, we used 512 samples from the base distribution  $\rho_0$ , a zero-centered Gaussian distribution with  $\sigma = 1$ . Fig. 2 illustrates the learned flow, or mass transport, from  $\rho_0$  to  $\rho_M$  by the CNF (Eq. 5) that minimizes  $E[\rho_M]$ ,  $N_e = 2$ . As we can also observe from Figs. 2-3, this CNF approach is capable of splitting the density given the large value of  $R$  and allocating a higher concentration of electron density closer to the Li nuclei. Our simulations indicate that only  $\sim 5,000$  optimization steps were needed for converged results, see Fig. S.1 in the SI.

We also explored the flexibility of our pro-

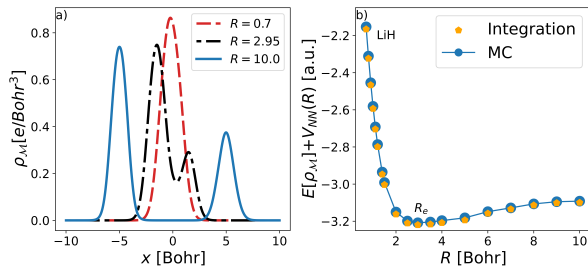


Figure 3: (a)  $\rho_{\mathcal{M}}$  for LiH for different nuclear distances  $R$ . For all simulations,  $\rho_0$  is a zero-centered Gaussian distribution with  $\sigma = 1$ . (b) The total energy of 1D LiH as a function of  $R$ .  $V_{\text{NN}}(R)$  is the nuclear repulsion term and  $R_e = 2.95$  a.u.  $\diamond$ -symbols represent the total energy value computed with trapezoidal rule, and  $\bullet$ -symbols with MC. See the text for more details of the simulations.

posed CNF framework by examining various inter-nuclear distances for LiH, as shown in Fig. 3. For these 1D simulations, we consistently employed the same  $\rho_0$ , a 1D Gaussian distribution centered at zero. The neural network (NN) architecture used for  $g_\phi$  featured three hidden layers, each with 512 neurons and the tanh activation function. Other architectures were tested but were found to be sub-optimal. Our simulations also reveal that  $g_\phi$ , when randomly initialized, effectively accelerates the minimization of  $E[\rho_{\mathcal{M}}]$ , particularly at large inter-nuclear distances ( $R \gg R_e$ ), where  $R_e = 2.95$  Bohr denotes the equilibrium bond distance. These results demonstrate the flexibility of  $g_\phi$  for different scenarios, from strong nuclear interactions ( $R < R_e$ ) to bond-breaking regimes ( $R \gg R_e$ ), Fig. 3. The potential energy surface curve for the LiH, Fig. 3, further corroborates these findings. We verified the validity of the proposed method by computing the total energy with the learned  $\rho_{\mathcal{M}}$  using quadrature integration, finding no discernible difference between Adam and RMSProp except when  $R \geq 6.0$  a.u. (Fig. S.1 and Table S.4 in the SI); however, in these 1D cases, RMSProp consistently achieves lower energy values (Table S.4 in the SI).

In normalizing flows, the transformation map

$T_\phi$  (Eq. 4) connects the base density,  $\rho_0$ , with the target density,  $\rho_\phi$ . While  $\rho_0$  is commonly modeled as a multi-variate Gaussian for applications like image generation, in the realm of molecular systems, adopting a promolecular density ( $\tilde{\rho}_0$ ), emerges as a more natural base distribution. This choice enhances the base model’s alignment with molecular structures and could potentially reduce the need for larger  $g_\phi$  models. Here, we define  $\tilde{\rho}_0 = \sum_i c_i \mathcal{N}_i(\mathbf{R}_i, \sigma = 1)$ , where  $\mathcal{N}_i$  is a 1S orbital centered at the nucleus position ( $\mathbf{R}_i$ ). The coefficients  $c_i$  represent the proportional influence of each nucleus on the overall density,  $\sum_i c_i = 1$ , and  $c_i = \frac{Z_i}{\sum_j Z_j}$  where  $Z_i$  is the atomic number of the  $i^{\text{th}}$ -nucleus. Other base distributions could be considered given the computation of the density and the score function is tractable and samples can be easily generated.

To precisely model this density transformation and account for symmetries in the system,  $g_\phi$  is a permutation equivariant graph neural network (GNN)<sup>74,75</sup>,

$$g_\phi(\mathbf{z}, t) = \sum_i^{N_a} f_\phi(\|\mathbf{z}(t) - \mathbf{R}_i\|_2, \tilde{Z}_i)(\mathbf{z}(t) - \mathbf{R}_i), \quad (10)$$

where  $N_a$  is the number of nuclei,  $\tilde{Z}_i$  is the atomic number of the  $i^{\text{th}}$ -nucleus encoded as a one-hot vector, and  $f_\phi$  is a  $M$ -layer NN with 64 neurons per layer, and the tanh activation function. This GNN architecture is selected for its capability to process permutations of input atoms invariantly, thereby capturing the molecule’s essential spatial and chemical properties, uninfluenced by the nuclei’s order. For  $\rho_{\mathcal{M}}$  to be permutation invariant with respect to the atoms, the vector field ( $g_\phi$ ) must be permutation equivariant, and  $\rho_0$  can be factorized across atoms, meaning permutation invariant<sup>48,75</sup>.

We further investigate the scalability of CNFs through simulations in realistic real-space systems, focusing on the  $\text{H}_2$ , LiH,  $\text{H}_2\text{O}$ , and four hydrocarbon molecules<sup>3</sup>. For these molecular systems, the exchange component of  $E_{\text{XC}}$  was modeled using a combination of the local density approximation and the B88 exchange functionals. For the correlation component  $E_{\text{C}}$ , we

<sup>3</sup>Simulations done on an NVIDIA V100 GPU.

utilized both the PW92<sup>76</sup> and the VWN<sup>77,78</sup> correlation functionals. Detailed equations are presented in the SI.

For  $\text{H}_2$  with  $R = 0.7 \text{ \AA}$ , we found that  $\sim 5,000$  iterations are needed for the total energy to stabilize, see Fig. 4. We further validate the total energy value using quadrature integration (MC), -1.2835 (-1.2798) a.u. for the VWN functional, and -1.2837 (-1.2799) a.u. for the PW92 functional. The difference between utilizing  $\rho_0$  or  $\tilde{\rho}_0$  in this diatomic system is minor, Fig. 4a. We also found a  $\sim 1 \text{ kcal/mol}$  energy difference when  $g_\phi$  with an additional layer is considered; see Table S.6 in the SI. Additionally, Figs. 4b and 4c illustrate the change of  $\rho_M$  through the optimization, notably showcasing an increase in the electron density around the nuclei. As a reference, the total energy for a KS-DFT simulation for the VWN functional with the 6-31G(d,p) (STO-3G) basis set is -1.6133 (-1.5917) a.u. The results for LiH are presented in Table S.6 in the SI.

For  $\text{H}_2\text{O}$ , the total energy stabilizes at  $\sim 8,000$  iterations when using  $\tilde{\rho}_0$ . As opposed to  $\text{H}_2$ , we found a significant improvement for water when a three-layer GNN was used without a big compromise in the optimization time (see Table S.6 in the SI). The total energy, computed with quadrature integration, for the VWN (PW92) functional, is -82.44516 (-82.48210) a.u. The results with  $\tilde{\rho}_0$  and the proposed  $g_\phi$  architecture (Eq. 10) agree with a KS-DFT simulation using a minimal basis set, which yielded -83.9016 a.u. This energy discrepancy is expected given the level of the KE functional used in the simulations. Additional information on the simulations is presented in the SI.

In normalizing flow-based models, the target density ( $\rho_\phi$ ) is derived by effectively “morphing” the base distribution into the target one. As the complexity of the diffeomorphism increases, a larger network is needed to capture accurately the  $\rho_0 \rightarrow \rho_\phi$  transformation. For the molecular systems studied in this work, as expected,  $T_\phi$  (Eq. 5) learns to primarily increase the electron density closer to the nucleus region, even if  $\rho_0$  has no previous knowledge of the location of the nucleus. This is illustrated in Fig. 5b, which displays  $\log |\det \nabla_{\mathbf{z}} T_\phi(\mathbf{z})|$  mapped over the base

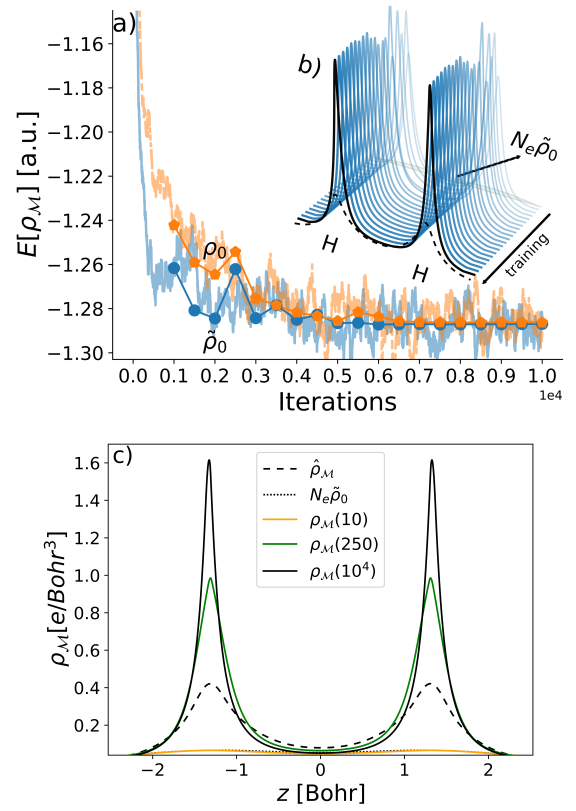


Figure 4: a) The total energy of  $\text{H}_2$  molecule through the optimization for a CNF with a single Gaussian distribution ( $\rho_0$ ) and a promolecular density ( $\tilde{\rho}_0$ ). The symbols indicate the total energy computed with quadrature integration and the curves with Monte Carlo. b) and c) The cross-section of the  $\rho_M$  at various iterations when  $\tilde{\rho}_0$  is used. For these simulations, used the PW92 functional for the correlation functional.  $\hat{\rho}_M$  represents the density computed using the KS formalism with a 6-31G(d,p) basis set.

distribution for the water molecule. Our findings indicate that in regions proximal to the nucleus,  $T_\phi$  effectively enhances electron density, as indicated by the sign of  $\log |\det \nabla_{\mathbf{z}} T_\phi(\mathbf{z})|$ . In contrast,  $T_\phi$  reduces the value of  $\rho_0$  in more distant areas, guaranteeing normalization. Fig. 5b further illustrates that  $T_\phi$  is unique for the base distribution used.

To assess the scalability of CNFs, we also considered benzene ( $\text{C}_6\text{H}_6$ ), anthracene ( $\text{C}_{14}\text{H}_{10}$ ), pyrene ( $\text{C}_{16}\text{H}_{10}$ ), and coronene ( $\text{C}_{24}\text{H}_{12}$ ) molecules. For these systems, we found Adam to be a more robust optimizer compared to



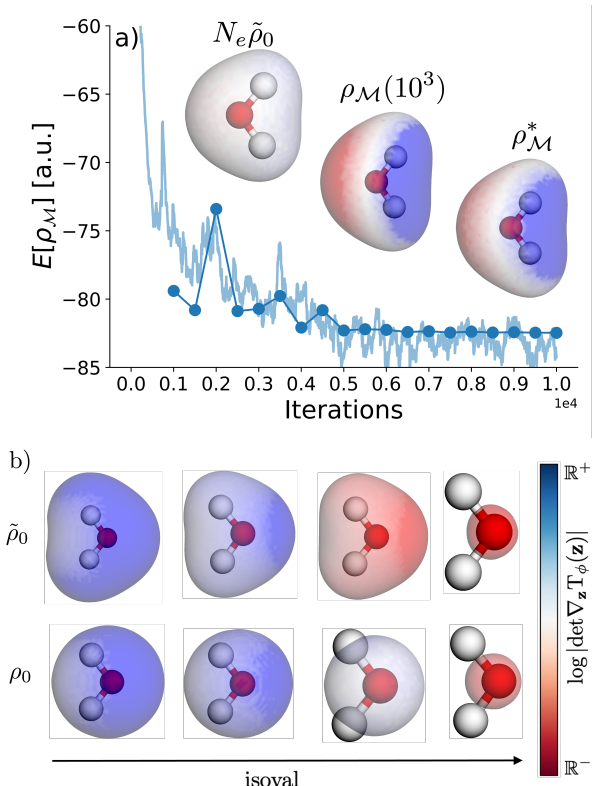


Figure 5: a) The total energy of  $\text{H}_2\text{O}$  molecule through the optimization for a CNF with a promolecular density ( $\tilde{\rho}_0$ ) as the base distributions. The symbols indicate the total energy computed with quadrature integration and the curves with Monte Carlo. For  $\rho_M$ , the color-coded map indicates the value of the molecular electrostatic potential, and  $\rho_M^*$  is the density with the lowest energy. b) The learned change of density ( $\log |\det \nabla_{\mathbf{z}} T_{\phi}(\mathbf{z})|$ ) by the CNF (Eq. 4) at different values of the base distribution;  $\rho_0$  is a single Gaussian distribution. For these simulations, we used the PW92 functional and a three-layer NN with 64 neurons per layer.

RMSProp, as the total energy computed using quadrature integration yields a lower value. The values of the total energies and training step times are reported in Table S.6 in the SI. We also observed that the total energy stabilizes at  $\sim 12,000$  iterations for these hydrocarbon molecules, see Fig. S.6 in the SI.

For benzene, the training step time is at least three times faster when  $\rho_0$  is a promolecular density. This can be observed in Fig. 6, where  $T_{\phi}$  locally updates  $\mathbf{x}$  around the nuclei, compared to the "long trajectory" required when

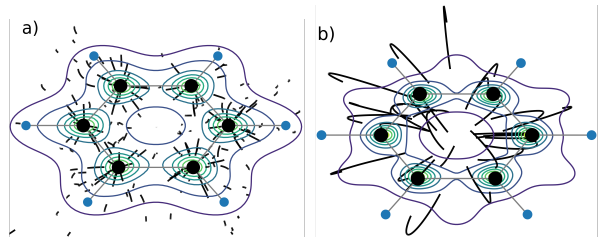


Figure 6: The trajectories learned by  $T_{\phi}$  for Benzene using the promolecular density (panel a) and a single Gaussian distribution (panel b) as base distributions. Each curve represents the transformation of  $\mathbf{z}$ , a random sample from the base distribution, to  $\mathbf{x}$ . The color contour plot represents the cross-section of the electron density parametrized by the CNF. In both simulations,  $g_{\phi}$  is a 4-layer GNN (Eq. 10) with 64 neurons per layer and the tanh activation function. The XC functional used was the PW92 functional.

$\rho_0$  is a single Gaussian distribution. We expect a similar trend for larger molecules given the complexity of distributing the density across more nuclei. For  $\text{C}_{14}\text{H}_{10}$ ,  $\text{C}_{16}\text{H}_{10}$ , and  $\text{C}_{24}\text{H}_{12}$ , the training step time ranges from 8 to 13 seconds per iteration for 3 layers and from 9 to 17 seconds for 4 layers. This iteration time depends on the batch size and the stiffness of the ODE in the backward pass. Only for coronene, our results indicate that a 3-layer GNN yields better results than one with an additional layer; this is due to the nature of the MC procedure, which is noisier for larger systems. We believe this could be alleviated using a multi-device approach, allowing the use of a larger number of samples from  $\tilde{\rho}_0$ , and employing ODE regularization schemes<sup>79–81</sup>. These limitations could inspire the development of additional tools for the proposed framework.

*Summary:* In this study, we introduce an innovative framework that utilizes generative models, particularly continuous normalizing flows, to parameterize electron densities in real space within molecular systems. This approach marks a significant shift away from traditional Lagrangian-based formulation within the OF-DFT framework. It distinguishes itself by ensuring direct normalization through the use of the change of

variable formula and merges the strengths of variational inference with modern approaches in machine learning optimization and automatic differentiation. Our methodology was tested across various chemical systems and combined with promolecular densities. This initialization step introduces prior physical knowledge into the model.

Furthermore, the integration of generative models into OF-DFT, along with the use of equivariant GNN, complemented by recent advancements in kinetic energy functional development<sup>22,82–89</sup>, holds a promising new avenue for the simulation of molecular systems. This different direction circumvents the limitations associated with grid-based methods, paving the way for alternative modeling of chemical systems within the OF-DFT framework in real space.

**Acknowledgement** The authors thank A. Aldossary, J. Davidsson, R. Armiento, and C. Benavides-Riveros for fruitful discussions. This research was enabled in part by support provided by the Digital Research Alliance of Canada and NSERC Discovery Grant No. RGPIN-RGPIN-2024-06594.

## References

- (1) Kohn, W.; Sham, L. J. Self-consistent equations including exchange and correlation effects. *Physical review* **1965**, *140*, A1133.
- (2) Becke, A. D. Perspective: Fifty years of density-functional theory in chemical physics. *The Journal of Chemical Physics* **2014**, *140*, 18A301.
- (3) Yu, H. S.; Li, S. L.; Truhlar, D. G. Perspective: Kohn-Sham density functional theory descending a staircase. *The Journal of Chemical Physics* **2016**, *145*, 130901.
- (4) Mardirossian, N.; Head-Gordon, M. Thirty years of density functional theory in computational chemistry: an overview and extensive assessment of 200 density functionals. *Molecular physics* **2017**, *115*, 2315–2372.
- (5) Mardirossian, N.; Head-Gordon, M. Thirty years of density functional theory in computational chemistry: an overview and extensive assessment of 200 density functionals. *Molecular Physics* **2017**, *115*, 2315–2372.
- (6) Teale, A. M. et al. DFT exchange: sharing perspectives on the workhorse of quantum chemistry and materials science. *Phys. Chem. Chem. Phys.* **2022**, *24*, 28700–28781.
- (7) Perdew, J. P.; Burke, K.; Ernzerhof, M. Generalized gradient approximation made simple. *Physical review letters* **1996**, *77*, 3865.
- (8) Stephens, P. J.; Devlin, F. J.; Chabalowski, C. F.; Frisch, M. J. Ab initio calculation of vibrational absorption and circular dichroism spectra using density functional force fields. *The Journal of physical chemistry* **1994**, *98*, 11623–11627.
- (9) Beck, A. D. Density-functional thermochemistry. III. The role of exact exchange. *J. Chem. Phys* **1993**, *98*, 5648–6.
- (10) Heyd, J.; Scuseria, G. E.; Ernzerhof, M. Hybrid functionals based on a screened Coulomb potential. *The Journal of chemical physics* **2003**, *118*, 8207–8215.
- (11) Borlido, P.; Schmidt, J.; Huran, A. W.; Tran, F.; Marques, M. A.; Botti, S. Exchange-correlation functionals for band gaps of solids: benchmark, reparametrization and machine learning. *npj Computational Materials* **2020**, *6*, 1–17.
- (12) Vargas-Hernández, R. A. Bayesian Optimization for Calibrating and Selecting Hybrid-Density Functional Models. *The Journal of Physical Chemistry A* **2020**, *124*, 4053–4061, PMID: 32338905.
- (13) Li, L.; Hoyer, S.; Pederson, R.; Sun, R.; Cubuk, E. D.; Riley, P.; Burke, K. Kohn-Sham Equations as Regularizer: Building Prior Knowledge into Machine-Learned Physics. *Phys. Rev. Lett.* **2021**, *126*, 036401.

- (14) Cuierrier, E.; Roy, P.-O.; Ernzerhof, M. Constructing and representing exchange–correlation holes through artificial neural networks. *The Journal of Chemical Physics* **2021**, *155*, 174121.
- (15) Wu, J.; Pun, S.-M.; Zheng, X.; Chen, G. Construct exchange-correlation functional via machine learning. *The Journal of Chemical Physics* **2023**, *159*, 090901.
- (16) Kirkpatrick, J.; McMorrow, B.; Turban, D. H.; Gaunt, A. L.; Spencer, J. S.; Matthews, A. G.; Obika, A.; Thiry, L.; Fortunato, M.; Pfau, D., et al. Pushing the frontiers of density functionals by solving the fractional electron problem. *Science* **2021**, *374*, 1385–1389.
- (17) Ma, H.; Narayanaswamy, A.; Riley, P.; Li, L. Evolving symbolic density functionals. *Science Advances* **2022**, *8*, eabq0279.
- (18) Hohenberg, P.; Kohn, W. Inhomogeneous electron gas. *Physical review* **1964**, *136*, B864.
- (19) Parr, R. G.; Yang, W. Density Functional Theory of Atoms and Molecules. Horizons of Quantum Chemistry. Dordrecht, 1980; pp 5–15.
- (20) Zhang, H.; Liu, S.; You, J.; Liu, C.; Zheng, S.; Lu, Z.; Wang, T.; Zheng, N.; Shao, B. Overcoming the barrier of orbital-free density functional theory for molecular systems using deep learning. *Nature Computational Science* **2024**, 1–14.
- (21) Karasiev, V. V.; Trickey, S. B. Issues and challenges in orbital-free density functional calculations. *Computer Physics Communications* **2012**, *183*, 2519–2527.
- (22) Mazo-Sevillano, P. d.; Hermann, J. Variational principle to regularize machine-learned density functionals: The non-interacting kinetic-energy functional. *The Journal of Chemical Physics* **2023**, *159*.
- (23) Hodges, C. Quantum corrections to the Thomas–Fermi approximation—the Kirzhnits method. *Canadian Journal of Physics* **1973**, *51*, 1428–1437.
- (24) Brack, M.; Jennings, B.; Chu, Y. On the extended Thomas-Fermi approximation to the kinetic energy density. *Physics Letters B* **1976**, *65*, 1–4.
- (25) Wang, L.-W.; Teter, M. P. Kinetic-energy functional of the electron density. *Physical Review B* **1992**, *45*, 13196.
- (26) Perrot, F. Hydrogen-hydrogen interaction in an electron gas. *Journal of Physics: Condensed Matter* **1994**, *6*, 431.
- (27) Wang, Y. A.; Govind, N.; Carter, E. A. Orbital-free kinetic-energy functionals for the nearly free electron gas. *Physical Review B* **1998**, *58*, 13465.
- (28) Huang, C.; Carter, E. A. Nonlocal orbital-free kinetic energy density functional for semiconductors. *Physical Review B* **2010**, *81*, 045206.
- (29) Smargiassi, E.; Madden, P. A. Orbital-free kinetic-energy functionals for first-principles molecular dynamics. *Physical Review B* **1994**, *49*, 5220.
- (30) Foley, M.; Madden, P. A. Further orbital-free kinetic-energy functionals for ab initio molecular dynamics. *Physical Review B* **1996**, *53*, 10589.
- (31) Mi, W.; Genova, A.; Pavanello, M. Non-local kinetic energy functionals by functional integration. *The Journal of Chemical Physics* **2018**, *148*.
- (32) Pedregosa, F. et al. Scikit-learn: Machine Learning in Python. *Journal of Machine Learning Research* **2011**, *12*, 2825–2830.
- (33) O’shea, K.; Nash, R. An introduction to convolutional neural networks. *arXiv preprint arXiv:1511.08458* **2015**,

- (34) He, K.; Zhang, X.; Ren, S.; Sun, J. Deep residual learning for image recognition. *Proceedings of the IEEE conference on computer vision and pattern recognition*. 2016; pp 770–778.
- (35) Alharbi, F. H.; Kais, S. Kinetic energy density for orbital-free density functional calculations by axiomatic approach. *International Journal of Quantum Chemistry* **2017**, *117*, e25373.
- (36) Fan, L.; Ziegler, T. Optimization of molecular structures by self-consistent and nonlocal density-functional theory. *The Journal of chemical physics* **1991**, *95*, 7401–7408.
- (37) Saad, Y.; Chelikowsky, J. R.; Shontz, S. M. Numerical methods for electronic structure calculations of materials. *SIAM review* **2010**, *52*, 3–54.
- (38) Schlegel, H. . Geometry optimization. *Wiley Interdisciplinary Reviews: Computational Molecular Science* **2011**, *1*, 790–809.
- (39) Thøgersen, L.; Olsen, J.; Yeager, D.; Jørgensen, P.; Sałek, P.; Helgaker, T. The trust-region self-consistent field method: Towards a black-box optimization in Hartree–Fock and Kohn–Sham theories. *The Journal of chemical physics* **2004**, *121*, 16–27.
- (40) David M. Blei, A. K.; McAuliffe, J. D. Variational Inference: A Review for Statisticians. *Journal of the American Statistical Association* **2017**, *112*, 859–877.
- (41) Lecun, Y.; Chopra, S.; Hadsell, R.; Ranzato, M.; Huang, F. In *Predicting structured data*; Bakir, G., Hofman, T., Scholkopt, B., Smola, A., Taskar, B., Eds.; MIT Press, 2006.
- (42) Teh, Y. W.; Welling, M.; Osindero, S.; Hinton, G. E. Energy-Based Models for Sparse Overcomplete Representations. *J. Mach. Learn. Res.* **2003**, *4*, 1235–1260.
- (43) Bu, L.-Z.; Wang, W. Efficient single-grid and multi-grid solvers for real-space orbital-free density functional theory. *Computer Physics Communications* **2023**, *290*, 108778.
- (44) Natarajan, B.; Casida, M. E.; Genovese, L.; Deutsch, T. Wavelets for density-functional theory and post-density-functional-theory calculations. *arXiv preprint arXiv:1110.4853* **2011**,
- (45) Chan, G. K.-L.; Cohen, A. J.; Handy, N. C. Thomas-Fermi-Dirac-von Weizsäcker models in finite systems. *The Journal of Chemical Physics* **2001**, *114*, 631–638.
- (46) Parr, R. G.; Bartolotti, L. J. Some remarks on the density functional theory of few-electron systems. *The Journal of Physical Chemistry* **1983**, *87*, 2810–2815.
- (47) Kobyzev, I.; Prince, S. J.; Brubaker, M. A. Normalizing flows: An introduction and review of current methods. *IEEE transactions on pattern analysis and machine intelligence* **2020**, *43*, 3964–3979.
- (48) Papamakarios, G.; Nalisnick, E.; Rezende, D. J.; Mohamed, S.; Lakshminarayanan, B. Normalizing flows for probabilistic modeling and inference. *The Journal of Machine Learning Research* **2021**, *22*, 2617–2680.
- (49) Rezende, D.; Mohamed, S. Variational inference with normalizing flows. *International conference on machine learning*. 2015; pp 1530–1538.
- (50) Cranmer, K.; Golkar, S.; Pappadopulo, D. Inferring the quantum density matrix with machine learning. *arXiv preprint arXiv:1904.05903* **2019**,
- (51) Saleh, Y.; Álvaro Fernández Corral;; Iske, A.; Küpper, J.; Yachmenev, A. Computing excited states of molecules using normalizing flows. 2023.
- (52) Thiede, L.; Sun, C.; Aspuru-Guzik, A. Waveflow: Enforcing boundary conditions in smooth normalizing flows with application to fermionic wave functions. *arXiv preprint arXiv:2211.14839* **2022**,



- (53) David, P.; Danilo, R. Integrable Nonparametric Flows. 2020.
- (54) James, S.; Brian, C.; Shravan, V. Numerical and geometrical aspects of flow-based variational quantum Monte Carlo. *Machine Learning: Science and Technology* **2023**, *4*, 021001.
- (55) Xie, H.; Zhang, L.; Wang, L. Ab-initio study of interacting fermions at finite temperature with neural canonical transformation. *arXiv preprint arXiv:2105.08644* **2021**,
- (56) Li, T.; Lin, M.; Hu, Z.; Zheng, K.; Vignale, G.; Kawaguchi, K.; Neto, A.; Novoselov, K. S.; Yan, S. D4FT: A Deep Learning Approach to Kohn-Sham Density Functional Theory. *arXiv preprint arXiv:2303.00399* **2023**,
- (57) Chen, R. T.; Rubanova, Y.; Bettencourt, J.; Duvenaud, D. K. Neural ordinary differential equations. *Advances in neural information processing systems* **2018**, *31*.
- (58) Chen, S.; Ding, S.; Karayiannidis, Y.; Björkman, M. Learning Continuous Normalizing Flows For Faster Convergence To Target Distribution via Ascent Regularizations. The Eleventh International Conference on Learning Representations. 2023.
- (59) Mohamed, S.; Rosca, M.; Figurnov, M.; Mnih, A. Monte carlo gradient estimation in machine learning. *Journal of Machine Learning Research* **2020**, *21*, 1–62.
- (60) Bradbury, J.; Frostig, R.; P.Hawkins,; Johnson, M.; Leary, C.; Maclaurin, D.; Necula, G.; Paszke, A.; VanderPlas, J.; Wanderman-Milne, S.; Zhang, Q. JAX: composable transformations of Python+NumPy programs. 2018; <http://github.com/google/jax>.
- (61) M. Casares, P. A.; Baker, J. S.; Medvidović, M.; Reis, R. d.; Arrazola, J. M. GradDFT. A software library for machine learning enhanced density functional theory. 2024; <https://doi.org/10.1063/5.0181037>.
- (62) Arrazola, J. M. et al. Differentiable quantum computational chemistry with PennyLane. 2023.
- (63) Kasim, M. F.; Vinko, S. M. Learning the Exchange-Correlation Functional from Nature with Fully Differentiable Density Functional Theory. *Phys. Rev. Lett.* **2021**, *127*, 126403.
- (64) Tamayo-Mendoza, T.; Kreisbeck, C.; Lindh, R.; Aspuru-Guzik, A. Automatic Differentiation in Quantum Chemistry with Applications to Fully Variational Hartree-Fock. *ACS Central Science* **2018**, *4*, 559–566, PMID: 29806002.
- (65) Vargas-Hernández, R. A.; Chen, R. T. Q.; Jung, K. A.; Brumer, P. Fully differentiable optimization protocols for non-equilibrium steady states. *New Journal of Physics* **2021**, *23*, 123006.
- (66) Vargas-Hernández, R. A.; Jorner, K.; Pollice, R.; Aspuru-Guzik, A. Inverse molecular design and parameter optimization with Hückel theory using automatic differentiation. *The Journal of Chemical Physics* **2023**, *158*, 104801.
- (67) Dawid, A. et al. Modern applications of machine learning in quantum sciences. 2023.
- (68) Zhang, X.; Chan, G. K.-L. Differentiable quantum chemistry with PySCF for molecules and materials at the mean-field level and beyond. *The Journal of Chemical Physics* **2022**, *157*, 204801.
- (69) Schmidt, J.; Benavides-Riveros, C. L.; Marques, M. A. Machine learning the physical nonlocal exchange-correlation functional of density-functional theory. *The journal of physical chemistry letters* **2019**, *10*, 6425–6431.
- (70) Tan, C. W.; Pickard, C. J.; Witt, W. C. Automatic differentiation for orbital-free

- density functional theory. *The Journal of Chemical Physics* **2023**, 158.
- (71) Costa, E.; Scriva, G.; Fazio, R.; Pilati, S. Deep-learning density functionals for gradient descent optimization. *Phys. Rev. E* **2022**, 106, 045309.
  - (72) Snyder, J. C.; Rupp, M.; Hansen, K.; Blooston, L.; Müller, K.; Burke, K. Orbital-free bond breaking via machine learning. *The Journal of chemical physics* **2013**, 139.
  - (73) Shulenburger, L.; Casula, M.; Senatore, G.; Martin, R. M. Spin resolved energy parametrization of a quasi-one-dimensional electron gas. *Journal of Physics A: Mathematical and Theoretical* **2009**, 42, 214021.
  - (74) Köhler, J.; Klein, L.; Noe, F. Equivariant Flows: Exact Likelihood Generative Learning for Symmetric Densities. Proceedings of the 37th International Conference on Machine Learning. 2020; pp 5361–5370.
  - (75) Zwartsenberg, B.; Scibior, A.; Niedoba, M.; Lioutas, V.; Sefas, J.; Liu, Y.; Dabiri, S.; Lavington, J. W.; Campbell, T.; Wood, F. Conditional Permutation Invariant Flows. *Transactions on Machine Learning Research* **2023**,
  - (76) Perdew, J. P.; Wang, Y. Accurate and simple analytic representation of the electron-gas correlation energy. *Physical review B* **1992**, 45, 13244.
  - (77) Vosko, S. H.; Wilk, L.; Nusair, M. Accurate spin-dependent electron liquid correlation energies for local spin density calculations: a critical analysis. *Canadian Journal of physics* **1980**, 58, 1200–1211.
  - (78) Shulenburger, L.; Casula, M.; Senatore, G.; Martin, R. M. Spin resolved energy parametrization of a quasi-one-dimensional electron gas. *Journal of Physics A: Mathematical and Theoretical* **2009**, 42, 214021.
  - (79) Kelly, J.; Bettencourt, J.; Johnson, M. J.; Duvenaud, D. Learning Differential Equations that are Easy to Solve. *Neural Information Processing Systems*. 2020.
  - (80) Kidger, P.; Chen, R. T. Q.; Lyons, T. J. "Hey, that's not an ODE": Faster ODE Adjoints via Seminorms. Proceedings of the 38th International Conference on Machine Learning. 2021; pp 5443–5452.
  - (81) Xu, C.; Cheng, X.; Xie, Y. Normalizing flow neural networks by JKO scheme. Thirty-seventh Conference on Neural Information Processing Systems. 2023.
  - (82) Zhang, H.; Liu, S.; You, J.; Liu, C.; Zheng, S.; Lu, Z.; Wang, T.; Zheng, N.; Shao, B. Overcoming the barrier of orbital-free density functional theory for molecular systems using deep learning. *Nature Computational Science* **2024**,
  - (83) Sun, L.; Chen, M. Machine-Learning-Based Non-Local Kinetic Energy Density Functional for Simple Metals and Alloys. *arXiv preprint arXiv:2310.15591* **2023**,
  - (84) Seino, J.; Kageyama, R.; Fujinami, M.; Ikabata, Y.; Nakai, H. Semi-local machine-learned kinetic energy density functional with third-order gradients of electron density. *The Journal of chemical physics* **2018**, 148.
  - (85) Fujinami, M.; Kageyama, R.; Seino, J.; Ikabata, Y.; Nakai, H. Orbital-free density functional theory calculation applying semi-local machine-learned kinetic energy density functional and kinetic potential. *Chemical Physics Letters* **2020**, 748, 137358.
  - (86) Manzhos, S.; Golub, P. Data-driven kinetic energy density fitting for orbital-free DFT: Linear vs Gaussian process regression. *The Journal of Chemical Physics* **2020**, 153.
  - (87) Seino, J.; Kageyama, R.; Fujinami, M.; Ikabata, Y.; Nakai, H. Semi-local machine-learned kinetic energy density functional demonstrating smooth potential energy

curves. *Chemical Physics Letters* **2019**, *734*, 136732.

- (88) Meyer, R.; Weichselbaum, M.; Hauser, A. W. Machine learning approaches toward orbital-free density functional theory: Simultaneous training on the kinetic energy density functional and its functional derivative. *Journal of chemical theory and computation* **2020**, *16*, 5685–5694.
- (89) Benavides-Riveros, C. L. Orbital-free quasi-density functional theory. *Physical Review Research* **2024**, *6*, 013060.

# Supplemental Material for "Leveraging Normalizing Flows for Orbital-Free Density Functional Theory"

Alexandre de Camargo,<sup>†</sup> Ricky T. Q. Chen,<sup>‡</sup> and Rodrigo

A. Vargas-Hernández<sup>\*,†,¶</sup>

<sup>†</sup> *McMaster University, Hamilton, ON, L8S 4M1, Canada*

<sup>‡</sup> *FAIR Meta, NY*

<sup>¶</sup> *Brockhouse Institute for Materials Research, McMaster University, Hamilton, ON, Canada*

E-mail: [vargashr@mcmaster.ca](mailto:vargashr@mcmaster.ca)

## Abstract

The purpose of this supplemental material is to provide more details about the proposed work in the main draft. Section 1 presents an introduction to normalizing flows, and Sections 2 and 3 describe the numerical details of the simulations and physical systems. In Section 4, we present additional results from the ones presented in the main text.

## 1 Normalizing Flows

The central goal of our work is to introduce an alternative parametrization for the electron density  $\rho_{\mathcal{M}}$  using normalizing flows (NFs)<sup>1</sup>,  $\rho_{\phi}$ . For convenience, we define  $\rho_{\mathcal{M}}$  as,

$$\rho_{\mathcal{M}}(\mathbf{x}) := N_e \rho_{\phi}(\mathbf{x}), \quad (1)$$

where  $\rho_\phi$  is also known as *shape factor*<sup>2,3</sup>. Eq. 1 guarantees the normalization to the number of electrons  $N_e$ , if  $\rho_\phi$  normalizes to one;  $\int \rho_\phi(\mathbf{x}) d\mathbf{x} = 1$ . As explained in the main text, we parametrize  $\rho_\phi$  using a normalizing flow<sup>1,4</sup>. Normalizing flows provides a general way of constructing complex probability distributions from simple ones, using the change of variable formula<sup>4</sup>,

$$\rho_\phi(\mathbf{x}) = \rho_0(\mathbf{z}) |\det \nabla_{\mathbf{z}} T_\phi(\mathbf{z})|^{-1}, \quad (2)$$

where  $T_\phi(\cdot)$  is a bijective differentiable transformation and  $\rho_0(\mathbf{z})$  is the base distribution. Eq. 2 guarantees volume preservation in the density transformation. One can parametrize  $T_\phi(\cdot)$  through a series of composable functions<sup>1,4,5</sup>,

$$T_\phi(\mathbf{z}) = (T_K \circ \dots \circ T_1)(\mathbf{z}). \quad (3)$$

These composable transformations can be seen as a flow discretized over time, and when multiple “layers” are considered it can parametrize further complex distributions.

## 1.1 Continuous Normalizing flow

An alternative formulation of (Eq. 2) is to construct a flow that operates in the continuous domain<sup>6,7</sup>, assuming that the state transition is governed by an ordinary differential equation (ODE). This alternative NF framework is called *continuous normalizing flow* (CNF), and it computes the  $T_\phi$ , the log density, and the score function by solving a joint ODE,

$$\partial_t \begin{bmatrix} \mathbf{z}(t) \\ \log \rho_\phi(\mathbf{z}(t)) \\ \nabla \log \rho_\phi \end{bmatrix} = \begin{bmatrix} \mathbf{g}_\phi(\mathbf{z}(t), t) \\ -\nabla_{\mathbf{x}} \cdot \mathbf{g}_\phi(\mathbf{z}(t), t) \\ -\nabla^2 \mathbf{g}_\phi - (\nabla \log \rho_\phi)^T (\nabla \mathbf{g}_\phi(\mathbf{z}(t), t)) \end{bmatrix}, \quad (4)$$

where “ $\nabla \cdot$ ” denotes the divergence operator,  $\nabla^2$  is  $\nabla \cdot \nabla$ , and  $\nabla_{\mathbf{x}} \log \rho(\mathbf{x})$  represents the score function<sup>7</sup>, which is relevant for computing  $\nabla_{\mathbf{x}} \rho(\mathbf{x})$  using the ”log-derivative trick”,

$$\nabla_{\mathbf{x}} \log \rho(\mathbf{x}) = \frac{\nabla_{\mathbf{x}} \rho(\mathbf{x})}{\rho(\mathbf{x})}. \quad (5)$$

We compute all required gradients by solving a second augmented ODE<sup>6</sup>. This approach applies to all ODE solvers and it’s called the adjoint sensitivity method<sup>8</sup>. For all results presented in this work, we used the mixed 4th/5th order Runge-Kutta integration method<sup>9</sup> implemented in `jax.experimental.ode.odeint`.

For the one-dimensional simulations, of the diatomic molecules, Section 4.1, the architecture of  $g_\phi$  is a standard feed-forward neural network (NN),

$$g_\phi(\mathbf{z}(t), t) = (f_M \circ \cdots \circ f_1)(\mathbf{z}(t), t), \quad (6)$$

where  $f_\ell(\cdot)$  is a linear layer followed by an activation function, and  $M$  is the number of layers. For the simulation in three dimensions, Section 4.2,  $g_\phi$  is parametrized by a permutation equivariant graph NN (GNN),<sup>10,11</sup>

$$g_\phi(\mathbf{z}, t) = \sum_i^{N_a} f_\ell(\|\mathbf{z}(t) - \mathbf{R}_i\|_2, \tilde{Z}_i)(\mathbf{z}(t) - \mathbf{R}_i), \quad (7)$$

where  $\tilde{Z}_i$  is the atomic number of the  $i^{th}$ -nucleus, encoded as a one-hot vector  $([0, \cdots, 1_i, \cdots, 0])$ ,  $N_a$  is the number of nucleus in the molecule, and  $f_\ell(\cdot)$  is a feed-forward NN with 64 neurons per layer, also with the tanh activation function. This GNN architecture was chosen due to its ability to handle the nuclei symmetries.

## 2 Expectation values of density functionals

In this section, we present the general framework used to compute the value of the total energy functional  $E[\rho_{\mathcal{M}}]$  for the one-dimensional and three-dimensional simulations portrayed in the main text. For any of the examples considered in this work, the total energy functional  $E[\rho_{\mathcal{M}}]$  is given by<sup>2,12</sup>,

$$E[\rho_{\mathcal{M}}] = T[\rho_{\mathcal{M}}] + V_{\text{H}}[\rho_{\mathcal{M}}] + V_{\text{e-N}}[\rho_{\mathcal{M}}] + E_{\text{XC}}[\rho_{\mathcal{M}}], \quad (8)$$

where we approximate the total kinetic energy ( $T[\rho_{\mathcal{M}}]$ ) by the sum of the Thomas-Fermi ( $T_{\text{TF}}[\rho_{\mathcal{M}}]$ ) and the Weizsäcker ( $T_{\text{W}}[\rho_{\mathcal{M}}]$ ) functionals<sup>2</sup>.  $V_{\text{H}}[\rho_{\mathcal{M}}]$  is the Hartree potential that describes the classical electron-electron repulsion,  $V_{\text{e-N}}[\rho_{\mathcal{M}}]$  is the external potential, and  $E_{\text{XC}}[\rho_{\mathcal{M}}]$  is the exchange-correlation (XC) functional<sup>2</sup>.

We use a Monte Carlo (MC) method to estimate the value of all individual functionals, through the following generalization,

$$F[\rho_{\mathcal{M}}] = \int f(\mathbf{x}, \rho_{\mathcal{M}}, \nabla \rho_{\mathcal{M}}) \rho_{\mathcal{M}}(\mathbf{x}) d\mathbf{x} = (\text{N}_{\text{e}})^p \int f(\mathbf{x}, \rho_{\phi}, \nabla \rho_{\phi}) \rho_{\phi}(\mathbf{x}) d\mathbf{x}, \quad (9)$$

where  $(\text{N}_{\text{e}})^p$ ,  $p \in \mathbb{R}$ , is the constant factor related to the number of electrons  $\text{N}_{\text{e}}$ , due to our definition of  $\rho_{\mathcal{M}}$  (Eq. 1), and  $f(\mathbf{x}, \rho_{\phi}, \nabla \rho_{\phi})$  is the integrand of the functional  $F[\rho_{\mathcal{M}}]$ . The expectation value of  $F[\rho_{\mathcal{M}}]$  is taken with respect to our base distribution  $\rho_0$ <sup>5</sup>,

$$F[\rho_{\mathcal{M}}] = (\text{N}_{\text{e}})^p \mathbb{E}_{\rho_0} [f(\text{T}_{\phi}(\mathbf{z}), \rho_{\phi}, \nabla \rho_{\phi})] \approx (\text{N}_{\text{e}})^p \frac{1}{N} \sum_{i=1}^N \mathbb{E}_{\rho_0} [f(\text{T}_{\phi}(\mathbf{z}_i), \rho_{\phi}, \nabla \rho_{\phi})], \quad (10)$$

where  $N$  is the samples drawn from  $\rho_0$  and transformed by the CNF, (Eq. 4); this is known as the reparameterization trick. In the following sections, we present the analytic expressions for each functional used in this work for the one-dimensional and three-dimensional cases.

## 2.1 One-dimensional density functionals

For the one-dimensional systems, the kinetic energy functional is the sum of the Thomas-Fermi  $(T_{\text{TF}}[\rho_{\mathcal{M}}])^{13}$  and the Weizsäcker  $(T_{\text{W}}[\rho_{\mathcal{M}}])^2$  functionals,

$$T_{\text{TF}}[\rho_{\mathcal{M}}] = \frac{\pi^2}{24} \int (\rho_{\mathcal{M}}(x))^3 dx \quad (11)$$

$$T_{\text{W}}[\rho_{\mathcal{M}}] = \frac{\lambda_0}{8} \int \frac{(\nabla \rho_{\mathcal{M}}(x))^2}{\rho_{\mathcal{M}}} dx = \frac{\lambda_0}{8} \int (\nabla \log \rho_{\mathcal{M}}(x))^2 \rho_{\mathcal{M}}(x) dx, \quad (12)$$

where the phenomenological parameter  $\lambda_0$  was set to 0.2<sup>14</sup>. For the  $V_{\text{H}}[\rho_{\mathcal{M}}]$  and  $V_{\text{e-N}}[\rho_{\mathcal{M}}]$  functionals, we used the soft approximation<sup>15</sup>,

$$V_{\text{H}}[\rho_{\mathcal{M}}] = \int \int \frac{\rho_{\mathcal{M}}(x) \rho_{\mathcal{M}}(x')}{\sqrt{1 + |x - x'|^2}} dx dx', \quad (13)$$

$$\begin{aligned} V_{\text{e-N}}[\rho_{\mathcal{M}}] &= \int v_{\text{e-N}}(x) \rho_{\mathcal{M}}(x) dx \\ &= - \int \left( \frac{Z_{\alpha}}{\sqrt{1 + |x - R/2|^2}} + \frac{Z_{\beta}}{\sqrt{1 + |x + R/2|^2}} \right) \rho_{\mathcal{M}}(x) dx, \end{aligned} \quad (14)$$

where  $Z_{\alpha}$  and  $Z_{\beta}$  are the atomic numbers and  $R$  is the distance between the two nuclei. The  $E_{\text{XC}}[\rho_{\mathcal{M}}]$  functional's form is given by<sup>16</sup>,

$$E_{\text{XC}}[\rho_{\mathcal{M}}] = \int \epsilon_{\text{XC}} \rho_{\mathcal{M}}(x) dx, \quad (15)$$

where  $\epsilon_{\text{XC}}$  is<sup>17</sup>,

$$\epsilon_{\text{XC}}(r_s, \zeta) = \frac{a_{\zeta} + b_{\zeta} r_s + c_{\zeta} r_s^2}{1 + d_{\zeta} r_s + e_{\zeta} r_s^2 + f_{\zeta} r_s^3} + \frac{g_{\zeta} r_s \ln[r_s + \alpha_{\zeta} r_s^{\beta_{\zeta}}]}{1 + h_{\zeta} r_s^2}. \quad (16)$$

For all one-dimensional simulations, we used,  $r_s = \frac{1}{2\rho_{\mathcal{M}}}$  (Wigner-Seitz radius<sup>17</sup>) and  $\zeta = 0$  (unpolarized density). All the parameters of  $\epsilon_{\text{XC}}$  are defined in Table S.1. The expectation



values of  $T_{\text{TF}}[\rho_{\mathcal{M}}]$ ,  $T_{\text{W}}[\rho_{\mathcal{M}}]$ ,  $V_{\text{H}}[\rho_{\mathcal{M}}]$ ,  $V_{\text{e-N}}[\rho_{\mathcal{M}}]$  and  $E_{\text{XC}}[\rho_{\mathcal{M}}]$ , accordingly to Eq. 10, are,

$$T_{\text{TF}}[\rho_{\mathcal{M}}] = \frac{\pi^2}{24} N_{\text{e}}^3 \mathbb{E}_{\rho_0} [(\rho_{\phi}(x))^2], \quad (17)$$

$$T_{\text{W}}[\rho_{\mathcal{M}}] = \frac{\lambda_0}{8} N_{\text{e}} \mathbb{E}_{\rho_0} \left[ \left( \frac{\nabla \rho_{\phi}(x)}{\rho_{\phi}(x)} \right)^2 \right] = \frac{\lambda_0}{8} N_{\text{e}} \mathbb{E}_{\rho_0} [(\nabla \log \rho_{\phi}(x))^2], \quad (18)$$

$$V_{\text{H}}[\rho_{\mathcal{M}}] = N_{\text{e}}^2 \mathbb{E}_{\rho_0} \left[ \frac{1}{\sqrt{1 + |x - x'|^2}} \right], \quad (19)$$

$$V_{\text{e-N}}[\rho_{\mathcal{M}}] = N_{\text{e}} \mathbb{E}_{\rho_0} \left[ -\frac{Z_{\alpha}}{\sqrt{1 + |x + R/2|^2}} - \frac{Z_{\beta}}{\sqrt{1 + |x + R/2|^2}} \right], \quad (20)$$

$$E_{\text{XC}}[\rho_{\mathcal{M}}] = N_{\text{e}} \mathbb{E}_{\rho_0} [\epsilon_{\text{XC}}(\mathbf{r}_{\text{s}}, \zeta)]. \quad (21)$$

Table 1: Parameter values of  $\epsilon_{\text{XC}}$  (Eq. 16) in a.u., obtained from Ref.<sup>17</sup>.

$a_0$	-0.8862269
$b_0$	-2.1414101
$c_0$	0.4721355
$d_0$	2.81423
$e_0$	0.529891
$f_0$	0.458513
$g_0$	-0.202642
$h_0$	0.470876
$\alpha_0$	0.104435
$\beta_0$	4.11613

## 2.2 Three-dimensional density functionals

In this section, we present the functionals used for the full three-dimensional simulations for the  $\text{H}_2$ ,  $\text{LiH}$ ,  $\text{H}_2\text{O}$ ,  $\text{C}_6\text{H}_6$ ,  $\text{C}_{14}\text{H}_{10}$ ,  $\text{C}_{16}\text{H}_{10}$  and  $\text{C}_{24}\text{H}_{12}$  molecules. The analytic forms of the

used density functionals are,

$$T_{\text{TF}}[\rho_{\mathcal{M}}] = \frac{3}{10}(3\pi^2)^{\frac{2}{3}} \int (\rho_{\mathcal{M}}(\mathbf{x}))^{5/3} d\mathbf{x}, \quad (22)$$

$$T_{\text{W}}[\rho_{\mathcal{M}}] = \frac{\lambda}{8} \int \frac{(\nabla \rho_{\mathcal{M}}(\mathbf{x}))^2}{\rho_{\mathcal{M}}(\mathbf{x})} d\mathbf{x} = \frac{\lambda}{8} \int (\nabla \log \rho_{\mathcal{M}}(\mathbf{x}))^2 \rho_{\mathcal{M}}(\mathbf{x}) d\mathbf{x}, \quad (23)$$

$$V_{\text{H}}[\rho_{\mathcal{M}}] = \frac{1}{2} \int \int \frac{\rho_{\mathcal{M}}(\mathbf{x}) \rho_{\mathcal{M}}(\mathbf{x}')}{\sqrt{|\mathbf{x} - \mathbf{x}'|^2}} d\mathbf{x} d\mathbf{x}', \quad (24)$$

$$V_{\text{e-N}}[\rho_{\mathcal{M}}] = \int v_{\text{e-N}}(\mathbf{x}) \rho_{\mathcal{M}}(\mathbf{x}) d\mathbf{x} = - \int \left( \sum_i \frac{Z_i}{\|\mathbf{x} - \mathbf{R}_i\|} \right) \rho_{\mathcal{M}}(\mathbf{x}) d\mathbf{x}, \quad (25)$$

where  $\mathbf{R}_i$  is the position of the  $i^{\text{th}}$ -nucleus. We took advantage of the "log-derivative trick" (Eq. 5) and defined  $T_{\text{W}}[\rho_{\mathcal{M}}]$  (Eq. 23) in terms on  $\nabla \log \rho_{\mathcal{M}}$ . Furthermore, the expectation values of the above functions (Eqs. 22–25) are,

$$T_{\text{TF}}[\rho_{\mathcal{M}}] = \frac{3}{10}(3\pi^2)^{\frac{2}{3}} N_{\text{e}}^{2/3} \mathbb{E}_{\rho_0} [\rho_{\phi}(\mathbf{x})], \quad (26)$$

$$T_{\text{W}}[\rho_{\mathcal{M}}] = \frac{\lambda}{8} N_{\text{e}} \mathbb{E}_{\rho_0} \left[ \left( \frac{\nabla \rho_{\phi}(\mathbf{x})}{\rho_{\phi}(\mathbf{x})} \right)^2 \right] = \frac{\lambda}{8} N_{\text{e}} \mathbb{E}_{\rho_0} [(\nabla \log \rho_{\phi}(\mathbf{x}))^2], \quad (27)$$

$$V_{\text{H}}[\rho_{\mathcal{M}}] = \frac{N_{\text{e}}^2}{2} \mathbb{E}_{\rho_0} \left[ \frac{1}{\sqrt{|\mathbf{x} - \mathbf{x}'|^2}} \right], \quad (28)$$

$$V_{\text{e-N}}[\rho_{\mathcal{M}}] = -N_{\text{e}} \mathbb{E}_{\rho_0} \left[ \sum_i \frac{Z_i}{\|\mathbf{x} - \mathbf{R}_i\|} \right], \quad (29)$$

The XC functional is composed of the sum of the exchange (X) and correlation (C) terms,

$$E_{\text{XC}}[\rho_{\mathcal{M}}] = \int \epsilon_{\text{XC}} \rho_{\mathcal{M}}(\mathbf{x}) d\mathbf{x} = \int \epsilon_{\text{X}} \rho_{\mathcal{M}}(\mathbf{x}) d\mathbf{x} + \int \epsilon_{\text{C}} \rho_{\mathcal{M}}(\mathbf{x}) d\mathbf{x}. \quad (30)$$

We report all different  $\epsilon_{\text{X}}$  and  $\epsilon_{\text{C}}$  used in the simulations,

$$\epsilon_{\text{X}}^{\text{LDA}} = -\frac{3}{4} \left( \frac{3}{\pi} \right)^{1/3} \rho_{\mathcal{M}}(\mathbf{x})^{1/3} \quad (31)$$

$$\epsilon_{\text{X}}^{\text{B88}} = -\beta \frac{X^2}{(1 + 6\beta X \sinh^{-1}(X))} \rho_{\mathcal{M}}(\mathbf{x})^{1/3}, \quad (32)$$

$$\epsilon_C^{\text{VWN}} = \frac{A}{2} \left\{ \ln \left( \frac{y^2}{Y(y)} \right) + \frac{2b}{Q} \tan^{-1} \left( \frac{Q}{2y+b} \right) + \right. \\ \left. - \frac{by_0}{Y(y_0)} \left[ \ln \left( \frac{(y-y_0)^2}{Y(y)} \right) + \frac{2(b+2y_0)}{Q} \tan^{-1} \left( \frac{Q}{2y+b} \right) \right] \right\} \quad (33)$$

$$\epsilon_C^{\text{PW92}} = -2A(1 + \alpha_1 r_s) \ln \left[ 1 + \frac{1}{2A(\beta_1 r_s^{1/2} + \beta_2 r_s + \beta_3 r_s^{3/2} + \beta_4 r_s^2)} \right] \quad (34)$$

where  $r_s = \left( \frac{3}{4\pi\rho_{\mathcal{M}}} \right)^{\frac{1}{3}}$  from Ref.<sup>18</sup>. For  $\epsilon_C^{\text{VWN}}$ ,  $y = r_s^{1/2}$ ,  $Y(y) = y^2 + by + c$ ,  $Q = \sqrt{4c - b^2}$ , and the constants  $b$ ,  $c$  and  $y_0$  are given in the Table S.2. The PW92's parameters are reported in Table S.3. For  $\epsilon_X^{\text{B88}}$ ,  $\beta$  is 0.0042 a.u. and  $X = \frac{|\nabla\rho_{\mathcal{M}}|}{\rho_{\mathcal{M}}^{4/3}}$ <sup>19</sup>, where we use the "log-derivative trick" (Eq. 5) and expand in terms of the score function  $X = \frac{|\rho_{\mathcal{M}} \nabla \log \rho_{\mathcal{M}}|}{\rho_{\mathcal{M}}^{4/3}}$ .

Table 2: Parameter values of  $\epsilon_C^{\text{VWN}}$  (Eq. 33) in a.u., obtained from Ref.<sup>20</sup>.

$A$	0.0621814
$y_0$	-0.10498
$b$	3.72744
$c$	12.9352

Table 3: Parameter values of  $\epsilon_C^{\text{PW92}}$  (Eq. 34) in a.u., obtained from Ref.<sup>18</sup>.

$A$	0.031091
$\alpha_1$	0.21370
$\beta_1$	7.5957
$\beta_2$	3.5876
$\beta_3$	1.6382
$\beta_4$	0.49294

### 3 Optimization algorithm

In this section, we present the optimization algorithm presented in the main text.

The optimization of  $\rho_{\mathcal{M}}$  was performed through an MC scheme where the parameters of the normalizing flow ( $\phi$ ) are updated via a stochastic gradient optimization,

$$\phi = \phi - \alpha \nabla_{\phi} E[\rho_{\mathcal{M}}], \quad (35)$$

where  $\alpha$  is the learning rate, and  $\nabla_{\phi} E[\rho_{\mathcal{M}}]$  is the gradient of the energy with respect to the parameters  $\phi$ . As mentioned in the main text,  $\nabla_{\phi} E[\rho_{\mathcal{M}}]$  is also estimated through a MC scheme<sup>21</sup>,

$$\nabla_{\phi} E[\rho_{\mathcal{M}}] = \mathbb{E}_{\rho_0}[\nabla_{\phi} f_E(\mathbf{T}_{\phi}(\mathbf{z}), \rho_{\phi}, \nabla \rho_{\phi})] \approx \frac{1}{N} \sum_i^N \nabla_{\phi} f_E(\mathbf{T}_{\phi}(\mathbf{z}_i), \rho_{\phi}(\mathbf{z}_i), \nabla_{\mathbf{z}_i} \rho_{\phi}). \quad (36)$$

For this work, all required gradients were computed using automatic differentiation, as it is a common practice in computational chemistry<sup>22–25</sup>.

The proposed algorithm is depicted in Algorithm 1. For all simulations, we employed RMSProp<sup>26</sup> and Adam<sup>27</sup> optimizers, featuring a learning rate schedule with initial and final values set at  $3 \times 10^{-4}$  and  $10^{-7}$ , respectively. Code was developed using JAX ecosystem<sup>28–30</sup>. The code developed for this work is available in the following repository.

---

**Algorithm 1** Optimization Algorithm

---

**Require:** CNF parameters  $\phi$ , base distribution  $\rho_0$ , energy functional  $E[\cdot]$

**while** not converged **do**

$\{\mathbf{z}_i, \log \rho_0(\mathbf{z}_i), \nabla_{\mathbf{z}} \log \rho_0(\mathbf{z}_i)\}_i^N \sim \rho_0(\mathbf{z})$  ▷ Sample the base distribution

$[\mathbf{x}_i, \log \rho_{\phi}(\mathbf{x}_i), \nabla_{\mathbf{x}} \log \rho_{\phi}(\mathbf{x}_i)] = \text{ODESolve}([\mathbf{z}_i, \log \rho_0(\mathbf{z}_i), \nabla_{\mathbf{z}} \log \rho_0(\mathbf{z}_i)], t_0, t_1, \phi)$  ▷ Solve ODE Eq.( 4)

$E = N_e^p \mathbb{E}_{\rho_{\phi}}[E[\mathbf{x}, \rho_{\mathcal{M}}, \nabla \rho_{\mathcal{M}}]] \approx \frac{N_e^p}{N} \sum_i^N f_E(\mathbf{x}_i, \rho_{\phi}(\mathbf{x}_i), \nabla \rho_{\phi}(\mathbf{x}_i))$  ▷ Compute energy, Eq. ( 9)

$\nabla_{\phi} E \approx \frac{(N_e)^p}{N} \sum_i^N \nabla_{\phi} f_E(\mathbf{x}_i, \rho_{\phi}(\mathbf{x}_i), \nabla \rho_{\phi}(\mathbf{x}_i))$  ▷ Evaluate gradients, Eq.( 36)

$\phi' = \text{optimizer step}(\phi, \nabla_{\phi} E)$  ▷ Update parameters

**end while**

**return** parameters  $\phi'$

---

## 4 Results

In this section, we present the results of the 1D and 3D simulations. The analytic equations of all functionals are presented in Sections 2.1 and 2.2, and Section 3 details the information of the optimization algorithm.

### 4.1 1D: LiH

In this section, we present additional results for the one-dimensional (1D) model of LiH at different inter-atomic distances ( $R$ ). For all simulations,  $g_\phi$  (Eq. 6) was parametrized by a three-layer neural network with 512 neurons per layer, and a tanh function. A maximum of 10,000 gradient iterations was allowed, and 512 samples from  $\rho_0$ . We only considered as based distribution  $\rho_0$  a 1D Gaussian distribution centered at 0;  $\mathcal{N}(0, \sigma = 1)$ .

The energy functional for different values of  $R$  was composed of the sum of  $T_{\text{TF}}[\rho_{\mathcal{M}}]$ ,  $T_{\text{W}}[\rho_{\mathcal{M}}]$ ,  $V_H[\rho_{\mathcal{M}}]$  and  $V_{\text{e-N}}[\rho_{\mathcal{M}}]$  (Eqs. 17-20). For the XC functional, we used the one from Ref.<sup>16</sup> (Eq. 16). In Fig. S.2, we presented the value of each functional through the optimization. To validate the total energy estimated with MC, we also used quadrature integration (trapezoidal rule). As observed, it follows the same trend as the estimated with MC. For low values of  $R$ , the optimization converges rapidly as the  $\rho_{\mathcal{M}}$  mimics a unimodal distribution. However, for larger values of  $R$ , a greater number of iterations is needed for  $g_\phi$  to split  $\rho_{\mathcal{M}}$  into a bimodal distribution. Fig S.1 compares the  $\rho_{\mathcal{M}}$  plots between RMSProp and Adam optimizers for various values of  $R$ . Finally, the RMSProp algorithm consistently achieves lower energy values for this 1D system at different values of  $R$ , see Table S.4. For all 1D simulations, we used an NVIDIA Tesla P100 GPU.

Table 4: The total energy, reported in Ha, is computed with MC and quadrature integration.  $\Delta\epsilon$  is the absolute difference of the energy, computed using trapezoidal rule, between both optimization algorithms.

	MC integration		Quadrature integration		
$R$ [a.u.]	Adam	RMSProp	Adam	RMSProp	$\Delta\epsilon$ [kcal/mol]
0.7	-4.16876	-4.16877	-4.178977	-4.178976	$8.90 \times 10^{-4}$
0.8	-4.14241	-4.14243	-4.152597	-4.152596	$4.62 \times 10^{-4}$
0.9	-4.11384	-4.11386	-4.123992	-4.123991	$6.50 \times 10^{-4}$
1.0	-4.08343	-4.08345	-4.093545	-4.093542	$1.71 \times 10^{-3}$
1.1	-4.05158	-4.05159	-4.06164	-4.06163	$2.14 \times 10^{-3}$
1.2	-4.01864	-4.01864	-4.02864	-4.02863	$3.55 \times 10^{-3}$
1.4	-3.95087	-3.95088	-3.960741	-3.960740	$2.36 \times 10^{-3}$
1.5	-3.91668	-3.91669	-3.9264736	-3.9264734	$6.09 \times 10^{-5}$
2.0	-3.75270	-3.75271	-3.762070	-3.762071	$3.26 \times 10^{-3}$
2.5	-3.61524	-3.61526	-3.624130	-3.624131	$2.58 \times 10^{-3}$
2.95	-3.52041	-3.52044	-3.528893	-3.528896	$1.69 \times 10^{-3}$
3.5	-3.43420	-3.43428	-3.44234	-3.44235	$5.32 \times 10^{-3}$
4.0	-3.37679	-3.37686	-3.3846610	-3.3846618	$5.20 \times 10^{-4}$
5.0	-3.30095	-3.30151	-3.30903	-3.30947	0.276
6.0	-3.25300	-3.21186	-3.26111	-3.25537	3.62
7.0	-3.14716	-3.19113	-3.1569	-3.18444	17.4
8.0	-3.15803	-3.15190	-3.16708	-3.16004	4.42
9.0	-3.14766	-3.12877	-3.15686	-3.17489	11.4
10.0	-3.11951	-3.12622	-3.12898	-3.13182	1.78

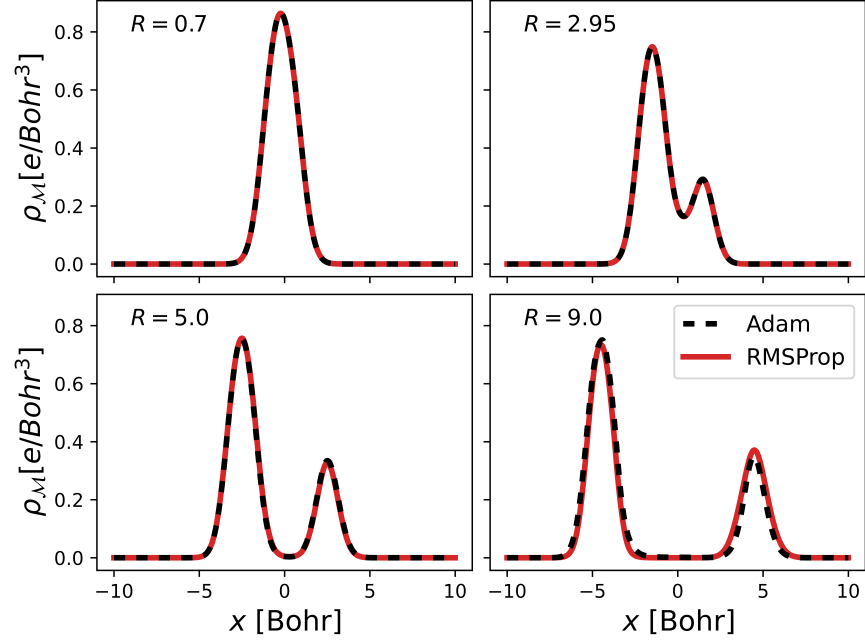


Figure 1: The plots of the electron density ( $\rho_M$ ), reported in electrons per cubic bohr, computed with RMSProp and Adam algorithms. Each panel shows the overlap between two independent simulations for different values of  $R$ .

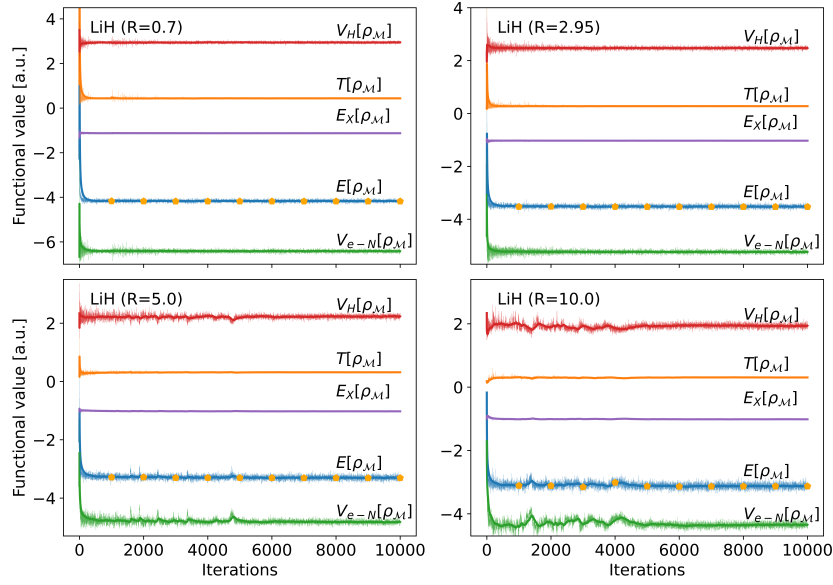


Figure 2: The value of the total energy and each functional, computed with MC (Eq. 10), at each iteration. Each panel represents an independent simulation for different values of  $R$ . The  $\blacklozenge$ -symbols represent the value of the total energy computed with quadrature integration. For all simulations, we used the same architecture for  $g_\phi$  and optimizer, see the text for more details.

## 4.2 3D:

In this section, we present additional results for the three-dimensional (3D) simulations for the  $\text{H}_2$ ,  $\text{LiH}$ ,  $\text{H}_2\text{O}$ ,  $\text{C}_6\text{H}_6$ ,  $\text{C}_{14}\text{H}_{10}$ ,  $\text{C}_{16}\text{H}_{10}$  and  $\text{C}_{24}\text{H}_{12}$  molecules. Only for the small molecules, we considered two distinct base distributions, (i) a single Gaussian distribution ( $\rho_0$ ), and (ii) a promolecular density ( $\tilde{\rho}_0$ ),

$$\tilde{\rho}_0 = \sum_i c_i \mathcal{N}_i(\mathbf{R}_i, \sigma = 1), \quad (37)$$

where  $\mathcal{N}_i(\cdot)$  is a 1S orbital centered at the nucleus position,  $\mathbf{R}_i$ . The coefficients  $c_i$  represent the proportional influence of each component on the overall density,  $c_i = \frac{Z_i}{\sum_j Z_j}$ , and it depends on  $Z_i$ , the atomic number of the  $i^{\text{th}}$ -nucleus. For the hydrocarbon molecules ( $\text{C}_x\text{H}_y$  molecules) we only consider a promolecular density. To account for possible symmetries in the  $V_{\text{e-N}}$  potential,  $\text{g}_\phi$  is a permutation equivariant graph neural network (GNN)<sup>10,11</sup>, Eq. 7. For all 3D simulations, we used an NVIDIA V100 GPU.

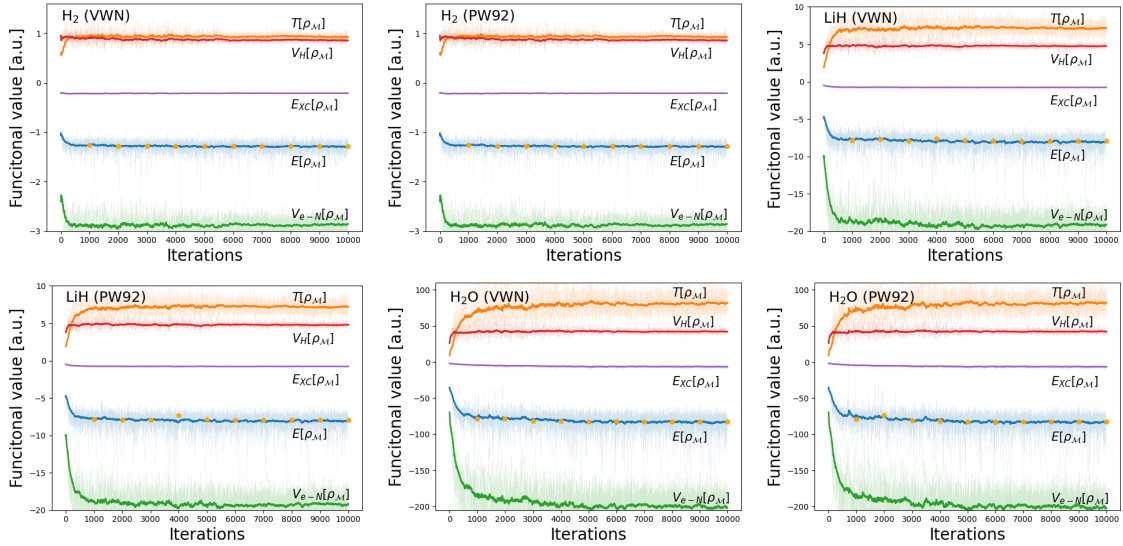


Figure 3: The value of  $E[\rho_{\mathcal{M}}]$  and each functional, computed with MC (Eq. 10), at each iteration of the optimization. In this case, we considered a promolecular density ( $\tilde{\rho}_0$ ) as our base distribution. The  $\blacklozenge$ -symbols represent the value of the total energy computed with quadrature integration. For all simulations, we used the same architecture for  $\text{g}_\phi$  and the RMSProp optimizer, see the text for more details.



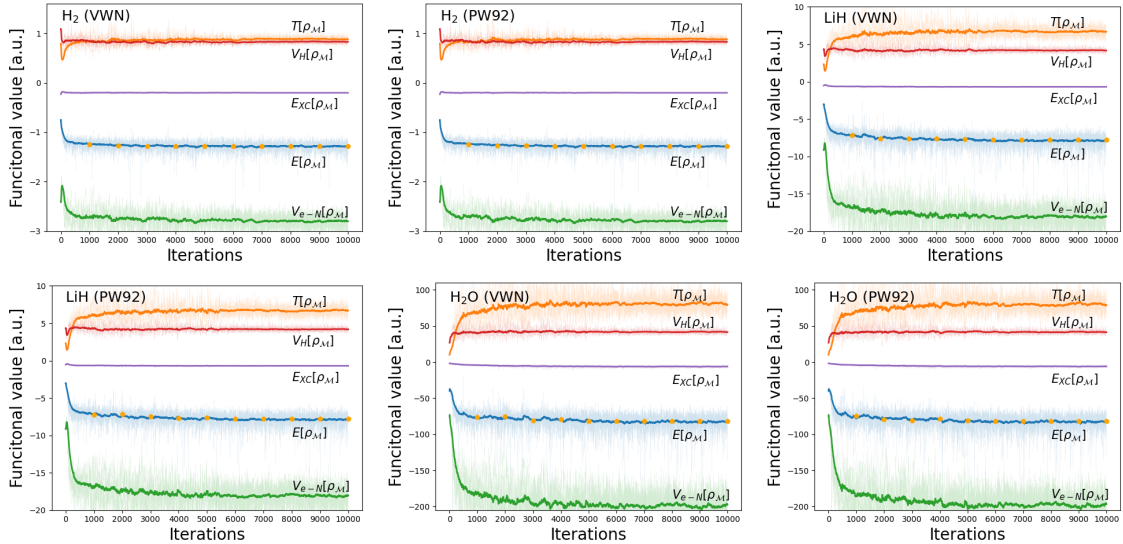


Figure 4: The value of  $E[\rho_M]$  and each functional, computed with MC (Eq. 10), at each iteration of the optimization. In this case, we considered a single Gaussian distribution ( $\rho_0$ ) as our base distribution. The  $\blacklozenge$ -symbols represent the value of the total energy computed with quadrature integration. For all simulations, we used the same architecture for  $g_\phi$  and the RMSProp optimizer, see the text for more details.

The total energy functional was composed of the sum of  $T_{TF}[\rho_M]$ ,  $T_W[\rho_M]$ ,  $V_H[\rho_M]$ , and  $V_{e-N}[\rho_M]$  (Eqs. 26-29). For the XC functional, we combine  $\epsilon_X^{LDA}$  and  $\epsilon_X^{B88}$ , Eqs. 31-32 respectively, as the exchange component, and intercalate  $\epsilon_C^{VWN}$  (Eq. 33) and  $\epsilon_C^{PW92}$  (Eq. 34) as the correlation term. Figs. S.3-S.4 show the value of each functional for H<sub>2</sub>, LiH, and H<sub>2</sub>O as a function of the iteration steps. For Fig. S.3, the base distribution was the promolecular density, and for Fig. S.4  $\rho_0$  was a single multi-variate Gaussian distribution. For both sets of simulations,  $g_\phi$ 's architecture (Eq. 7) comprised three layers. Fig. S.5 shows the value of the total energy ( $E[\rho_M]$ ) as a function of the iteration steps for the hydrocarbon molecules ( $C_xH_y$  molecules) using the promolecular density. For this set of simulations,  $g_\phi$ 's architecture (Eq. 7) comprised four layers.

Table S.6 contains the total energy values of all molecular systems considered here for the VWN and PW92 functionals using the promolecular density. For all systems, we considered multiple layers to examine the impact of having a  $g_\phi$  with more layers. We also report the average iteration step time using a minibatch size of 512 for the small molecules and 724 for

the hydrocarbon molecules ( $C_xH_y$  molecules). For bigger systems, we found that the training procedure reaches an equilibrium after  $\sim 12,000$  training steps, as observed in Fig. S.5. To validate the proposed methodology, we computed the total energy employing quadrature integration methods used in DFT packages<sup>31</sup>. These results are also presented in Table S.6.

To verify the normalization of  $\rho_{\mathcal{M}}$ , we also used quadrature integration methods to compute the difference with respect to the  $N_e$ ,

$$\Delta N_e = \int \rho_{\mathcal{M}}(\mathbf{x}) d\mathbf{x} - N_e. \quad (38)$$

Fig. S.6 shows the value of  $\Delta N_e$  for the small molecules and Table S.5 reported the absolute value of  $\Delta N_e$  for the  $C_xH_y$  molecules.

Table 5: The absolute value of  $\Delta N_e$  (Eq. 38) for the hydrocarbon molecules ( $C_xH_y$  molecules).

		Adam		RMSPProp	
Molecule ( $N_e$ )	# Layers	VWN	PW92	VWN	PW92
$C_6H_6$ (42) benzene	3	$5.0 \times 10^{-5}$	$7.5 \times 10^{-5}$	$5.3 \times 10^{-5}$	$9.4 \times 10^{-5}$
	4	$2.7 \times 10^{-5}$	$1.1 \times 10^{-5}$	$3.8 \times 10^{-5}$	$3.5 \times 10^{-5}$
$C_{14}H_{10}$ (96) anthracene	3	$6.4 \times 10^{-5}$	$5.5 \times 10^{-5}$	$1.8 \times 10^{-4}$	$1.5 \times 10^{-4}$
	4	$1.4 \times 10^{-4}$	$1.9 \times 10^{-4}$	$1.1 \times 10^{-4}$	$1.7 \times 10^{-4}$
$C_{16}H_{10}$ (106) pyrene	3	$1.0 \times 10^{-4}$	$8.7 \times 10^{-5}$	$2.7 \times 10^{-4}$	$2.9 \times 10^{-4}$
	4	$2.4 \times 10^{-4}$	$2.1 \times 10^{-4}$	$4.9 \times 10^{-4}$	$5.1 \times 10^{-4}$
$C_{24}H_{12}$ (156) coronene	3	$6.9 \times 10^{-4}$	$6.5 \times 10^{-4}$	$6.3 \times 10^{-4}$	$6.0 \times 10^{-4}$
	4	$7.2 \times 10^{-4}$	$9.5 \times 10^{-4}$	$7.9 \times 10^{-4}$	$8.4 \times 10^{-4}$

Total energy MC integration				Total energy quadrature integration				Iteration time [s]	
Molecule (N <sub>e</sub> )	# Layers	Adam		RMSProp		Adam		RMSProp	
		VWN	PW92	VWN	PW92	VWN	PW92	VWN	PW92
H <sub>2</sub> (2)	1	-1.28043	-1.28040	-1.28038	-1.28045	-1.27668	-1.27665	-1.27666	-1.27674
	2	-1.28860	-1.28854	-1.28811	-1.28823	-1.28501	-1.28504	-1.28463	-1.28475
	3	-1.29075	-1.29078	-1.29053	-1.29055	-1.28716	-1.28723	-1.28703	-1.28704
LiH (4)	1	-7.95421	-7.95479	-7.94972	-7.95175	-7.84666	-7.84684	-7.84346	-7.84428
	2	-8.06433	-8.05864	-8.05514	-8.06152	-7.95530	-7.95300	-7.95066	-7.95185
	3	-8.07509	-8.07257	-8.06180	-8.06198	-7.96105	-7.96297	-7.96081	-7.96262
H <sub>2</sub> O (10)	1	-79.76794	-79.70309	-79.58261	-79.57113	-78.59261	-78.57637	-78.40929	-78.37367
	2	-82.77371	-82.91470	-82.80063	-82.77893	-81.96175	-82.16772	-82.00596	-81.96604
	3	-83.23742	-83.38899	-83.27477	-83.25400	-82.44516	-82.48210	-82.41970	-82.38154
C <sub>6</sub> H <sub>6</sub> (42) benzene	3	-409.84658	-409.63297	-410.44893	-410.17949	-408.46554	-408.49605	-409.26159	-409.05600
	4	-410.61044	-410.03415	-413.74284	-413.60553	-409.47686	-409.19518	-412.29239	-412.17791
C <sub>14</sub> H <sub>10</sub> (96) anthracene	3	-1219.39095	-1216.54545	-1201.12833	-1203.82600	-1216.8759	-1214.16513	-1198.22969	-1200.47439
	4	-1227.42202	-1227.93900	-1217.00866	-1215.75897	-1224.91707	-1225.25808	-1213.72391	-1212.40638
C <sub>16</sub> H <sub>10</sub> (106) pyrene	3	-1485.36895	-1481.67124	-1462.95408	-1460.88932	-1480.2493	-1477.8062	-1459.9878	-1457.1779
	4	-1488.20147	-1491.04825	-1481.22059	-1481.20265	-1484.54730	-1487.03938	-1476.59673	-1475.88246
C <sub>24</sub> H <sub>12</sub> (156) coronene	3	-2601.68518	-2604.28162	-2541.68127	-2545.02514	-2581.70553	-2583.91283	-2519.84625	-2523.29440
	4	-2601.88376	-2602.41654	-2560.61346	-2560.74780	-2580.25980	-2580.03025	-2538.83560	-2537.96701

Table 6: The total energy, reported in Ha, computed with MC and quadrature integration for two different XC functionals. For the MC values, we averaged the lowest 300 energy points. We also reported the average iteration-step time in seconds.

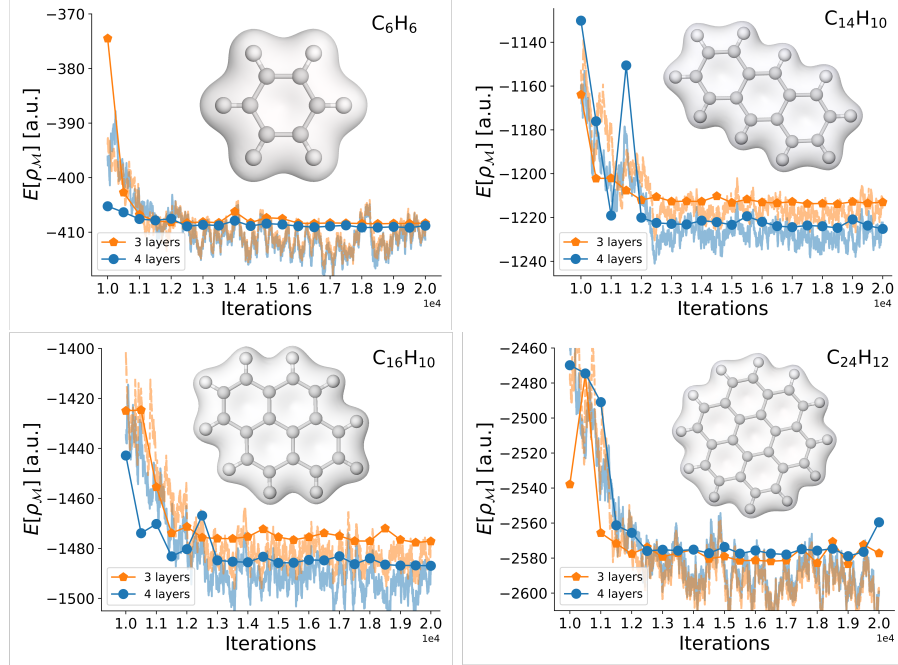


Figure 5: The total energy of the molecule through the optimization for a CNF with a promolecular density ( $\tilde{\rho}_0$ ). The symbols indicate the total energy computed with quadrature integration and the curves with Monte Carlo. For these simulations, we considered a GNN (Eq. 7) with 3 (◆) and 4 layers (●) with 64 neurons per layer, the PW92 functional and Adam optimizer. We also display the electron density parametrized with a CNF with the lowest total energy computed with quadrature integration.

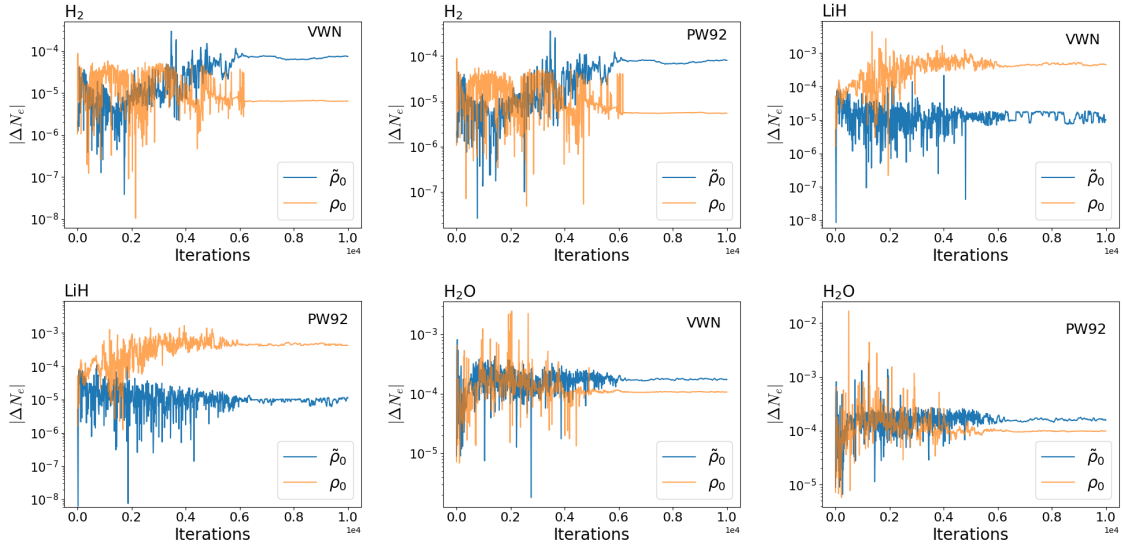


Figure 6: The absolute difference between the number of electrons ( $N_e$ ) and the integral of  $\rho_M$  at each iteration during the optimization.

## References

- (1) Kobyzev, I.; Prince, S. J.; Brubaker, M. A. Normalizing flows: An introduction and review of current methods. *IEEE transactions on pattern analysis and machine intelligence* **2020**, *43*, 3964–3979.
- (2) Parr, R. G.; Yang, W. Density Functional Theory of Atoms and Molecules. Horizons of Quantum Chemistry. Dordrecht, 1980; pp 5–15.
- (3) Parr, R. G.; Bartolotti, L. J. Some remarks on the density functional theory of few-electron systems. *The Journal of Physical Chemistry* **1983**, *87*, 2810–2815.
- (4) Papamakarios, G.; Nalisnick, E.; Rezende, D. J.; Mohamed, S.; Lakshminarayanan, B. Normalizing flows for probabilistic modeling and inference. *The Journal of Machine Learning Research* **2021**, *22*, 2617–2680.
- (5) Rezende, D.; Mohamed, S. Variational inference with normalizing flows. International conference on machine learning. 2015; pp 1530–1538.
- (6) Chen, R. T.; Rubanova, Y.; Bettencourt, J.; Duvenaud, D. K. Neural ordinary differential equations. *Advances in neural information processing systems* **2018**, *31*.
- (7) Chen, S.; Ding, S.; Karayiannidis, Y.; Björkman, M. Learning Continuous Normalizing Flows For Faster Convergence To Target Distribution via Ascent Regularizations. The Eleventh International Conference on Learning Representations. 2023.
- (8) Pontryagin, L. S. *Mathematical theory of optimal processes*; Routledge, 2018.
- (9) Shampine, L. F. Some practical runge-kutta formulas. *Mathematics of computation* **1986**, *46*, 135–150.
- (10) Köhler, J.; Klein, L.; Noe, F. Equivariant Flows: Exact Likelihood Generative Learning for Symmetric Densities. Proceedings of the 37th International Conference on Machine Learning. 2020; pp 5361–5370.

- (11) Zwartsenberg, B.; Scibior, A.; Niedoba, M.; Lioutas, V.; Sefas, J.; Liu, Y.; Dabiri, S.; Lavington, J. W.; Campbell, T.; Wood, F. Conditional Permutation Invariant Flows. *Transactions on Machine Learning Research* **2023**,
- (12) Hohenberg, P.; Kohn, W. Inhomogeneous electron gas. *Physical review* **1964**, *136*, B864.
- (13) Snyder, J. C.; Rupp, M.; Hansen, K.; Blooston, L.; Müller, K.; Burke, K. Orbital-free bond breaking via machine learning. *The Journal of chemical physics* **2013**, *139*.
- (14) Chan, G. K.-L.; Cohen, A. J.; Handy, N. C. Thomas-Fermi-Dirac-von Weizsäcker models in finite systems. *The Journal of Chemical Physics* **2001**, *114*, 631–638.
- (15) Snyder, J. C.; Rupp, M.; Hansen, K.; Müller, K.-R.; Burke, K. Finding density functionals with machine learning. *Physical review letters* **2012**, *108*, 253002.
- (16) Helbig, N.; Fuks, J. I.; Casula, M.; Verstraete, M. J.; Marques, M. A.; Tokatly, I.; Rubio, A. Density functional theory beyond the linear regime: Validating an adiabatic local density approximation. *Physical Review A* **2011**, *83*, 032503.
- (17) Shulenburger, L.; Casula, M.; Senatore, G.; Martin, R. M. Spin resolved energy parametrization of a quasi-one-dimensional electron gas. *Journal of Physics A: Mathematical and Theoretical* **2009**, *42*, 214021.
- (18) Perdew, J. P.; Wang, Y. Accurate and simple analytic representation of the electron-gas correlation energy. *Physical review B* **1992**, *45*, 13244.
- (19) Becke, A. D. Density-functional exchange-energy approximation with correct asymptotic behavior. *Physical review A* **1988**, *38*, 3098.
- (20) Vosko, S. H.; Wilk, L.; Nusair, M. Accurate spin-dependent electron liquid correlation energies for local spin density calculations: a critical analysis. *Canadian Journal of physics* **1980**, *58*, 1200–1211.

- (21) Mohamed, S.; Rosca, M.; Figurnov, M.; Mnih, A. Monte carlo gradient estimation in machine learning. *Journal of Machine Learning Research* **2020**, *21*, 1–62.
- (22) M. Casares, P. A.; Baker, J. S.; Medvidović, M.; Reis, R. d.; Arrazola, J. M. GradDFT. A software library for machine learning enhanced density functional theory. 2024; <https://doi.org/10.1063/5.0181037>.
- (23) Kasim, M. F.; Vinko, S. M. Learning the Exchange-Correlation Functional from Nature with Fully Differentiable Density Functional Theory. *Phys. Rev. Lett.* **2021**, *127*, 126403.
- (24) Tamayo-Mendoza, T.; Kreisbeck, C.; Lindh, R.; Aspuru-Guzik, A. Automatic Differentiation in Quantum Chemistry with Applications to Fully Variational Hartree–Fock. *ACS Central Science* **2018**, *4*, 559–566, PMID: 29806002.
- (25) Vargas–Hernández, R. A.; Jorner, K.; Pollice, R.; Aspuru–Guzik, A. Inverse molecular design and parameter optimization with Hückel theory using automatic differentiation. *The Journal of Chemical Physics* **2023**, *158*, 104801.
- (26) Tieleman, T.; Hinton, G., et al. Lecture 6.5-RMSProp: Divide the gradient by a running average of its recent magnitude. *COURSERA: Neural networks for machine learning* **2012**, *4*, 26–31.
- (27) Kingma, D. P.; Ba, J. Adam: A method for stochastic optimization. *arXiv preprint arXiv:1412.6980* **2014**,
- (28) Bradbury, J.; Frostig, R.; P.Hawkins,; Johnson, M.; Leary, C.; Maclaurin, D.; Necula, G.; Paszke, A.; VanderPlas, J.; Wanderman-Milne, S.; Zhang, Q. JAX: composable transformations of Python+NumPy programs. 2018; <http://github.com/google/jax>.
- (29) Heek, J.; A.Levskaya,; Oliver, A.; Ritter, M.; Rondepierre, B.; Steiner, A.; van Zee, M. Flax: A neural network library and ecosystem for JAX. 2023; <http://github.com/google/flax>.

- (30) DeepMind, et al. The DeepMind JAX Ecosystem. 2020; <http://github.com/deepmind>.
- (31) Becke, A. D. A multicenter numerical integration scheme for polyatomic molecules. *The Journal of chemical physics* **1988**, 88, 2547–2553.